Live 3D imaging and mapping of shear stresses within tissues using incompressible elastic beads

Alexandre Souchaud[1], Arthur Boutillon[2], Gaëlle Charron[1], Atef Asnacios[1], Camille Nous[3], Nicolas B. David[2], Francois Graner[1,*] and Francois Gallet[1,*]

[1]Matière et Systèmes Complexes, UMR 7057 associée au CNRS et à l'Université de Paris, 10 rue Alice Domon et Léonie Duquet, 75013 Paris, France.
[2]Laboratory for Optics and Biosciences, Ecole Polytechnique, CNRS, INSERM, Institut Polytechnique de Paris, 91128 Palaiseau, France.
[3]Laboratory Cogitamus, France
*Authors for correspondence Email: francois.gallet@u-paris.fr; francois.graner@u-paris.fr

Abstract

To investigate the role of mechanical constraints in morphogenesis and development, we develop a pipeline of techniques based on incompressible elastic sensors. These techniques combine the advantages of incompressible liquid droplets, which have been used as precise *in situ* shear stress sensors, and of elastic compressible beads, which are easier to tune and to use. Droplets of a polydimethylsiloxane (PDMS) mix, made fluorescent through specific covalent binding to a rhodamin dye, are produced by a microfluidics device. The elastomer rigidity after polymerization is adjusted to the tissue rigidity. Its mechanical properties are carefully calibrated *in situ*, for a sensor embedded in a cell aggregate submitted to uniaxial compression. Thelocal shear stress tensor is retrieved from the sensor shape, accurately reconstructed through an active contour method. *In vitro*, within cell aggregates, and *in vivo*, in the prechordal plate of the Zebrafish embryo during gastrulation,our pipeline of techniques demonstrates its efficiency to directly measure the three dimensional shear stress repartition within a tissue.

Keywords: Mechanical stress, elastic gel, sensor, PDMS, cell aggregate, Zebrafish

INTRODUCTION

The cohesion and morphogenesis of living tissues require coordinated processes at the cellular scale, based on changes in cell number, size, shape, position and packing (Heisenberg and Bellaïche, 2013; Guirao et al., 2015). These rearrangements are possible because cells can generate and exert mechanical stresses on their surroundings, or conversely feel the stresses and transduce them into biological signals. The complete process is thus regulated under the dual control of genetics and mechanics, which mutually feedback on each other, and drive the growth and shape of tissues (Desprat et al., 2008). Hence, the impact of mechanics on tissue fate and organization is considerable, either for healthy organisms during embryo development (Krieg et al., 2008; Le Goff et al., 2013; Heisenberg and Bellaïche, 2013; Hiramatsu et al., 2013; Hamada, 2015; Herrera-Perez and Karen, 2018), or in pathological conditions (Wells, 2013; Delarue et al., 2014b; Angeli and Stylianopoulos, 2016). Quantitative studies about the role ofmechanical constraints in morphogenesis and development benefit from a precise and quantitative knowledge of the spatial distribution of

mechanical stresses, from the subcellular scale to the tissue scale, and of its temporal evolution.

In the past decades numerous methods have been developed in order to achieve *in situ* stress measurements, using different and complementary techniques; for reviews see Sugimura et al. (2016); Campàs (2016); Roca-Cusachs et al. (2017); Gomez-Gonzalez et al. (2020). To summarize, these techniques can be classified into approximately four categories: (i) External contact manipulations, including micropipettes (Mitchison and Swann, 1954; Hochmuth, 2000; Von Dassow et al., 2010; Guevorkian et al., 2010), microplates (Desprat et al., 2005; Mitrossilis et al., 2009; Tinevez et al., 2009; Mgharbel et al., 2009), AFM indentation (Butt et al., 2005; Elkin et al., 2007; Xiong et al., 2009; Franze, 2011; Lau et al., 2015), traction force microscopy (TFM) (Nier et al., 2016); (ii) Manipulations using light, comprising laser ablation (Rauzi et al., 2008; Bonnet et al., 2012; Porazinski et al., 2015) and optical tweezers (Neuman and Nagy, 2008; Bambardekar et al., 2015) - and also by extent magnetic tweezers (Hosu et al., 2003; Tanase et al., 2007; Mazuel et al., 2015); (iii) Non-contact optical imaging, in which one can find birefringence (Nienhaus et al., 2009; Schluck and Aegerter, 2010) and stress inference (Chiou et al., 2012; Ishihara et al., 2013; Brodland et al., 2014; Roffay et al., 2021); and finally (iv) Embedded local sensors, from FRET at the molecular scale (Grashoff et al., 2010; Borghi et al., 2012) to microsensors at the cell scale (Campàs et al., 2014; Dolega et al., 2017; Mongera et al., 2018; Mohagheghian et al., 2018; Lee et al., 2019; Träber et al., 2019).

The latter technique based on microsensors is quantitative, barely perturbative, and suitable to monitor tissue stresses at the scale of a cell or a group of cells. Two main avenues have already been explored.

The pioneer article (Campàs et al., 2014) has used incompressible liquid droplets to measure the shear stress tensor, which is the most important stress component to understand how anisotropic forces govern tissue morphogenesis. The droplet synthesis and manipulation, as well as the data analysis, is atour de force. Liquid microdroplets, made of fluorocarbon oil, have been injected in aggregates of mesenchymal cells, in living mandible explants. Coating the oil surface with a biocompatible surfactant enables the droplet insertion in the tissue. The mechanical stresses exerted by the surrounding cells modify the droplet shape, and the deviation from the average stress normal to the droplet surface can be calculated from its local curvature, according to Laplace's law. Calibration of the liquid/tissuesurface tension enables direct measurements of the three-dimensional (3D) components and orientations of the shear stress tensor. The same group proposed an alternative use of liquid droplets as actuators to probe the tissue mechanical properties (instead of stress), and applied it to Zebrafish embryos (Mongera et al., 2018).

Other groups have favored elastic beads because they are easier to produce, tune, calibrate, manipulate, insert in tissues, and analyze. The stress exerted on a solid sensor by surrounding cells can be deduced from its deformation, provided that the elastic moduli are determined through an independent calibration. Inspired by Matrigel pressure sensors (Monnier et al., 2016), sensors have been prepared using polyacrylic acid (PAA) hydrogels (Dolega et al., 2017; Lee et al., 2019; Träber et al., 2019), whose Young modulus can be tuned from 60 to 4000 Pa (Lee et al., 2019), or alginate gels (Mohagheghian et al., 2018), and injected in cell aggregates or Zebrafish embryos. Water can flow in and out of an hydrogel, making it compressible. In principle this method yields access to the total stress, that is, simultaneously the compression stress (including osmotic pressure contributions) and shear stress. The rest state for each sensor without stress can be determined at the end of the experiment by lysing the cells; once the compression stress is determined, the shear stress can be estimated by substraction (Mohagheghian et al., 2018).

To combine the chemical and mechanical advantages of incompressible liquid droplets, namely fluorescence, functionalization, and accurate shear stress measurements, with the ease to tune and use compressible solid beads, we develop a pipeline of techniques based on incompressible solid beads of diameter comparable to the cell size. The material must exhibit a well-defined elastic behavior, with a Young modulus comparable to the one of the surrounding tissue (order of magnitude 10^3 Pa), in order to get a measurable deformation under physiological stresses, which expected order of magnitude is e.g. 10^2 Pa in zebrafish development (Mongera et al., 2018). Coating of the sensors surface is necessary to make them biocompatible and to make their insertion non-perturbative. To observe the sensor's deformation and get a precise 3D reconstruction of its shape, a stable fluorescent labelling is also needed.

Our choice fell on polydimethylsiloxane (PDMS), which is an elastic elastomer, with a Young modulus adjustable down to a few hundred Pa (Hobbie et al., 2008). Production of small droplets of PDMS polymerisable mixture, having a fixed diameter, can be easily controlled through a microfluidic device. We introduce a novel method to bind the elastomer to a fluorescent dye through covalent bonds, leading to a stable, homogeneous and high intensity fluorescence. Coating the PDMS with cell adhesion proteins should also be possible, as mentioned in the literature (Toworfe et al., 2004; Schneider et al., 2011). The sensors can be embedded in the tissue in a non-perturbative way, and their deformation followed over minutes or hours. For 3D image analysis, we implement an active contour method algorithm to determine the shapeof the deformed sensors. This method leads to direct and accurate measurements of the 3D components and orientations of the shear stress tensor. This contrasts with the use of compressible hydrogel sensors, which is mainly sensitive to the local pressure inside the tissue, and the shear stress is deduced by subtraction from the total stress. When only the shear stress measurement is required, using incompressible PDMS sensors is easier and more precise.

The technique was successfully tested in two different systems, *in vitro* and *in vivo*. First, reconstituted cell aggregates were chosen as a tumor model, for which it is well known that mechanical constraints have a major influence on the organization and fate (Delarue et al., 2014b; Northcott et al., 2018). Moreover, it is relatively easy to produce aggregates with embedded sensors, which makes it a privileged system to validate the method. Second, we investigated the distribution of mechanical constraints in the prechordal plate of the Zebrafish embryo during its development. Indeed, based on *in vitro* observation, it has been postulated that anisotropies and heterogeneities of mechanical stresses are present in the prechordal plate, and are of importance to guide its migration (Weber et al., 2012; Behrndt and Heisenberg, 2012). However, due to the lack of appropriate tools, the existence of such anisotropies could not be directly tested so far. The implantation of our mechanical sensors in this system could help to definitively decide between different models actually disputed.

In both cases, *in vitro* and *in vivo*, we report here results concerning the spatial repartition of the shear stresses, providing clear demonstration of the usability and potential of these new sensors.

Methods

The above requirements can be summarized as follows: the sensors must have a size comparable to the cell size, and be easily fabricated and manipulated in large quantities; they must be biocompatible and conveniently embedded in living tissues; their rigidity has to be homogeneous and close to those of the tissues; they can be fluorescently labelled in a homogeneous and stable way; their 3D shape can be precisely reconstructed with minimal

effort; the effective shear modulus of the sensors can be reliably calibrated *in situ*; the shear stress tensor can be decoupled from compression stress and directly derived from the 3D sensor's deformations by using linear elasticity; shear stresses of order of 10^2 Pa can be measured with 10 Pa sensitivity. To satisfy simultaneously all these constraints, we introduce the following pipeline of techniques.

Microsensors fabrication

The microsensors were made out of a silicon elastomer similar to usual PDMS. The polymerizable mix preparation is first dispersed into liquid droplets of about $30\ \mu m$ in size, thanks to a microfluidic circuit, and afterwards polymerized at $80 m 1^\circ C$. Briefly, the main component of the elastomer is vinyl terminated polydimethylsiloxane, hereafter coined DMS. It is mixed with a polymeric hydrosilane (methylhydrosiloxane-dimethylsiloxane copolymer) that acts as a cross-linker via hydrosilylation of the vinyl ends of DMS (Fig. S1a). The ratio of cross-linker to DMS must be carefully controlled ($m_{cross} = 1.60 \times 10^{-2}\ m_{DMS}$) to achieve the desired shear modulus after polymerisation. The hydrosilylation reaction is initiated using Karstedt's catalyst ($m_{catal} = 4.286 \times 10^{-3}\ m_{DMS}$). A divinylic inhibitor (diallyl maleate) is also added ($m_{inhib} = 0.8571 \times 10^{-3}\ m_{DMS}$) to slow down the reaction kinetics. The as-prepared mixture needs to be stored at 4° C and should be used within a few days least the cross-linking reaction significantly moves forward.

Dispersing the polymerizable mix into spherical droplets of homogeneous size is obtained through a custom-made microfluidic circuit, by a classical flow focusing method (Haejune, 2007). The dispersed phase (polymer mix) meets the carrier phase (water) at a 4-channels crossing, and the resulting droplets suspension is collected at the output. The rectangular channel section is about $50 \times 20\ \mu m^2$. The injecting pressures of both phases is finely tuned and regulated by a Fluigent controller, in order to get a steady-state dripping instability and a constant droplet diameter. This diameter may be tuned between 20 and $40\ \mu m$. It is stable for a given droplet batch: the diameter distribution of droplets is quite monodisperse within a same production (Fig. 1). The monodispersity is not necessary for shear stress measurements. In the present work, the monodispersity facilitates the calibration. Moreover, it allows to identify possible optical artefacts during image analysis (see Section **Results**): we discarded images of beads with a measured radius out of the expected range.

The droplets polymerization into spherical elastic beads is achieved by baking the suspension at $80^\circ C$ during $3\ h$. The final gel is very soft. It sticks easily and irreversibly to any wall, including inert surfaces like teflon or silanized glass. Thus one must avoid the contact of the droplets with any solid surface during and after polymerization. To achieve this, the beaker containing the suspension is placed during baking on a turntable, rotating at about one turn per second. Since the gel is less dense than water, buoyancy makes the polymerized beads spontaneously concentrate at the center of the meniscus of the water free surface. Then, the concentrated suspension containing about 10^4 beads per mL can be collected with a micropipette, aliquoted in Eppendorf tubes and immediately stored in a freezer at $-20^\circ C$. The beads remain stable for weeks at this temperature, and are thawed before immediate use.

Fluorescent labelling

In order to observe the sensors embedded in the tissue, a dye must be added to the elastomer. The objective is to get an homogeneous fluorescent signal, with high enough intensity, to be able to visualize the sensors with usual 3D fluorescent microscopy techniques (confocal, spinning-disk and 2-photon microscopies) and to precisely reconstruct their 3D shape. Several hydrophobic dyes did not lead to satisfying labelling: either the dye could not be homogeneously dispersed in the polymer mix (fluorescein diacetate), or it was partially released in the water solution surrounding the beads, so that the fluorescent signal rapidly decreased with time (Nile Red and Cryptolyte™). We also attempted to label the elastomer with quantum dots (QDs) dispersed in the mixture. However, despite some specific coating to make them hydrophobic, QDs remained partially aggregated and the dispersion was not complete.

For efficient fluorescent labelling of the elastomer, two challenges needed to be overcome: the dye had to easily disperse into the polymerisable mix and, once dispersed and after curing, should not escape the meshwork of the gel and leak into the surroundings. Our strategy entailed attachment of the organic dye to the cross-linker via a parallel hydrosilylation reaction (Fig. S1b). The dye therefore needed to bear a vinyl terminal group. Isothiocyanate-bearing fluorophores can be conveniently modified through quantitative C-N bond formation. We selected Rhodamine B isothiocyanate because of its emission in the red and condensed it with allylamine to give a vinyl-terminated rhodamine B analogue (Fig. S1c). The compound was then added to DMS in a molar ratio of one fluorophore for 1,000 DMS strands (see Supporting Information for details).

Figure 2 shows some examples of bright field and fluorescent images of single sensors (a) suspended in water; (b) embedded in a CT26 reconstituted aggregate; (c) implanted in a Zebrafish embryo. Image (b2) is a 3D reconstruction obtainedwith ImageJ software, where the deformation from spherical shape is clearly visible. The fluorescent signal is homogeneous in the bead volume and the contrast is high enough to detect the sensor border (see section **Active contour method**). Moreover, we checked that the fluorescence in the elastomer remains stable over several days. Thus this labelling technique fulfills all the requirements for further quantitative image analysis.

Strain-stress relationship

When a bead is embedded in a tissue, it experiences mechanical forces exerted by its environment, which induce a deformation from its initial spherical shape, and makes it a sensor of local stresses. In the following we assume that the sensor is small enough, as compared to the length scale characterizing stress spatial variations, so that the stress tensor can be considered as homogeneous over the sensor's volume. Thus, stress variations at a scale smaller than the sensor cannot be detected. We also assume that the elastomer shows an ideally elastic behavior, and that its deformation remains small enough ($\lesssim 5\%$), so that linear elasticity applies. The local strain tensor $\bar{\bar{\varepsilon}}$ and stress tensor $\bar{\bar{\sigma}}$ are related through (Landau et al., 1986):

$$\bar{\bar{\varepsilon}} = \frac{1+\nu}{E}\bar{\bar{\sigma}}_d + \frac{1-2\nu}{E}\bar{\bar{\sigma}}_c \qquad (1)$$

Here $\bar{\bar{\sigma}}^c = \frac{tr(\bar{\bar{\sigma}})}{3}1$ represents the isotropic part of $\bar{\bar{\sigma}}$ (traction stress tensor, i.e. the pressure is $-\sigma_c$) and $\bar{\bar{\sigma}}^d = \bar{\bar{\sigma}} - \bar{\bar{\sigma}}^c$ isthe deviator, also known as shear stress tensor; E is the Young modulus, and ν the Poisson's ratio.
The sensors are made out of a PDMS elastomer, which can be considered as incompressible in the range of physiological stresses (its compression modulus $K = \frac{E}{1-2\nu}$ is of the order of 10^6 Pa). This justifies the approximation $\nu \approx 0.5$, and thus Eq. 1 simplifies into $\bar{\bar{\varepsilon}} = \frac{1+\nu}{E}\bar{\bar{\sigma}}^d$. Introducing the shear modulus $\mu = \frac{E}{2+2\nu} = \frac{E}{3}$, one gets:

$$\bar{\bar{\sigma}}^d = 2\mu\bar{\bar{\varepsilon}} \tag{2}$$

which we will use in the following.
Under external stresses, and assuming small deformations, the sensor's shape changes from a sphere of radius a to an ellipsoid of half-axes a_X, a_Y and a_Z. In the system of principal coordinates (X, Y, Z) of this ellipsoid, both the strain and stress tensors are diagonal, so that one can write:

$$\sigma^d_{XX} = 2\mu\varepsilon_{XX} = 2\mu\frac{(a_X - a)}{a} \tag{3}$$

$$\sigma^d_{XY} = 2\mu\varepsilon_{XY} = 0 \tag{4}$$

and similar relations for other stress components. Hence, provided that the shear modulus of the PDMS elastomer has been independently calibrated, the local shear stress tensor is fully determined by pointing the ellipsoid orientation and measuring the length of its half-axes. Note that the accuracy of the image analysis process allowed us to determine the ellipsoidal shape; but not small-scale deviations from it, related to possible variations of the stress tensor at a scale smaller than the sensor's size.

Cell culture and preparation of aggregates

CT26 cells, stably transfected with Lifeact-GFP, were cultivated in T75 flasks at $37^\circ C$ in 5% CO_2, in DMEM culture medium completed with 10% (v/v) Foetal Bovine Serum and 1% antibiotics (penicillin-streptomycin), and passed every 3 days. For the preparation of aggregates, confluent cells were detached by using $5\ mL$ of buffer solution containing 0.05% trypsin. Incubation was limited to about $1\ min$, in order to form cell leaflets and avoid complete cell dispersion. In parallel, elastomer microsensors were functionalized by adding $1\ mL$ of fibronectin solution in PBS ($50\ \mu g/mL$) to $1\ mL$ of freshly thawed bead suspension. The final suspension was left for incubation during $1\ h$ at $37^\circ C$, and then directly added to $\sim 10\ mL$ of detached cells suspension without further rinsing. Aggregates containing inserted beads were prepared in Petri dishes on which the cell and bead suspension was deposited, placed on an orbital agitator (~ 50 rotations/min), and left to grow for at least $24\ h$ in an incubator at $37^\circ C$. To get spherical aggregates, it is suitable to let them

grow for at least 48 h. The diameter of the obtained aggregates lies between 100 and 500 µm. Within few exceptions, they contain at most one bead per aggregate.

Zebrafish preparation

Embryos were obtained by natural spawning of *Tg(-1.8 gsc:GFP)ml1* adult fishes (Doitsidou et al., 2002). All animal studies were approved by the Ethical Committee N°59 and the Ministére de l'Education Nationale, de l'Enseignement Supérieur et de la Recherche under the file number APAFIS#15859-2018051710341011v3.

Embryos were grown at 28.5°C until reaching shield stage (6 hours post fertilization). Embryos were then processed as explained in Boutillon et al. (2018). Using a large glass needle (35 µm opening) mounted on a pneumatic microinjector (Narishige IM-11-2) under a fluorescence-stereo microscope, a sensor was inserted in the shield of an embryo, which expresses GFP in the *Tg(-1.8 gsc:GFP)ml1* line. Transplanted embryos were then incubated at 28.5°C until reaching the desired stage between 60% and 85% of epiboly (6,5 to 8 hours post fertilization). Embryos were then selected for the presence of the sensor in the prechordal plate. In our hands, this represented about 50% of transplanted embryos. In the others, the sensor was either not in the prechordal plate or had been expelled out of the embryo. Selected embryos were mounted in 0,2% agarose in embryo medium on the glass coverslip of a MatTek Petri dish (Boutillon et al., 2018) and placed on an inverted TCS SP8 confocal microscope (Leica SP8) equipped with an environmental chamber (Life Imaging Services) at 28°C and a HC PL APO 40x/1.10 W CS2 objective (Leica). Imaging parameters were set to acquire the whole sensor (z-stack) in less than 15 seconds, to minimize displacement due to the migrating neighboring cells.

Image recording and analysis

Microscopy

To simultaneously image the tissue and the sensors embedded inside it, several techniques have been used:

(i) Frequently, sensors in suspension in water were imaged with a spinning-disk microscope (Andor Revolution CSU X1, mounted on an Olympus IX 81 inverted microscope equiped with a 40x water immersion objective), in order to check their sphericity, and the good quality of their fluorescence (intensity and homogeneity) (Fig. 2a).

(ii) 2-photon microscopy was used for the visualization of reconstituted cell aggregates. Experiments were carried out at the multiphoton facility of the ImagoSeine imaging platform (Institut Jacques Monod, Université de Paris). The aggregates were deposited in a Petri dish, in a chamber regulated at 37°C, and observed during a few hours under a 20x water immersion objective at the early stage of their adhesion to the bottom plate. For the rhodamin dye, the excitation laser was tuned at $\lambda = 840$ nm and the emitted light was collected through a dichroïc mirror at $\lambda \geq 585$ nm. Lifeact-GFP of CT26 cells was excited at $\lambda = 900$ nm and the fluorescence was collected at $\lambda \leq 585$ nm. Image stacks were recorded along the optical axis every 0.5 µm, with a lateral resolution down to 0.1 μm / pixel (Fig. 2b).

(iii) A confocal microscope (Leica SP8) was used to image the prechordal plate of the Zebrafish embryos. The sample was maintained at $T = 28^{\circ}\mathrm{C}$. Image stacks (40x water immersion objective) were recorded at regular time intervals (30 s to $1\mathrm{min}$) at different stages of the epiboly, comprised between 60 and 85%. Since the prechordal plate is migrating at a velocity up to $2\ \mu\mathrm{m/min}$, the acquisition time for a whole stack must be smaller than 15 s to avoid drift in the images. Hence images were recorded every $2\ \mu\mathrm{m}$. The excitation laser was tuned at $\lambda = 498$ and $550\ \mathrm{nm}$ and the emitted light was collected between $507 - 537\ \mathrm{nm}$ and $569 - 673\ \mathrm{nm}$ (Fig. 2c).

Active contour method

A careful 3D reconstruction of the sensor's shape was required to retrieve the orientation and half-axes of the deformed beads with a good accuracy. Indeed, the usual built-in applications for 3D reconstructions, such as ImageJ plugins, do not lead to a reliable and accurate enough profile: the result depends on specific choices of parameters for the filters and for the intensity thresholds, which involve the subjective appreciation of the operator. Hence, we implemented an active contour method, as follows (Kass et al., 1988; Caselles et al., 1993; Marquez-Neila et al., 2014; Bendaoud, 2017): the common principle of the different existing algorithms consists in considering a swelling (or shrinking) surface $\nu(s,n)$ at the n^{th} iterative stage, parametrized by its local coordinates $s = (s_1, s_2)$. A function $E(\nu)$ is associated to this surface and, like an energy, is built to reach a minimum when the surface $\nu(s,n)$ coïncides with the contour of the object. This pseudo-energy is the sum of three contributions:

$$E(\nu) = E_g(\nu) + E_s(\nu) + E_c(\nu) \tag{5}$$

The first term $E_g(\nu)$ is a gradient detection term:

$$E_g(\nu) = -\iint \left\| \vec{\nabla}(g_\sigma * I) \right\|^2 ds \tag{6}$$

It represents the norm of the intensity gradient, convoluted by a gaussian filter g_σ, and integrated over the surface ν. The minus sign ensures that $E_g(\nu)$ has a minimum when the intensity gradient on the surface ν is maximal.

The second term (surface energy) $E_s(\nu)$, is analogous to a Helfrich energy (Helfrich, 1973):

$$E_s(\nu) = \iint \alpha\, ds + \iint \beta\kappa\, ds \tag{7}$$

where α is a surface tension, κ the local curvature of the surface ν, and β a curvature stiffness. This term limits the roughness of the final contour.
The last term (balloon energy) $E_b(\nu)$ is proportional to the volume V limited by ν, and forces the surface to swell or to shrink when iterating the process, according to the sign of the parameter δ :

$$E_b(\nu) = \delta \iiint dV \tag{8}$$

The details of the used Python code can be found in Souchaud (2020) and on the Github platform (see **Data availability**). Starting from a seed located inside the contour to be detected, and taking $\delta < 0$, the volume delimited by ν enlarges at each step n of the algorithm, until $E(\nu)$ reaches a minimum, which defines the contour of the object. The principle of the method is illustrated in Figure 3a, and an example of contour determination for a micro-sensor is shown in Figure 3b. A movie (M1) showing the 3D reconstruction of a bead inserted in the prechordal plate of a Zebrafish embryo is available in Supporting Information. Consequently, the final contour position only depends on the choice of δ and of two parameters α_1 and β_1 derived from α and β. In the algorithm, δ is an integer and must be equal to -1 to ensure convergence. We have checked that tuning α_1 and β_1 in a large range (variations up to 100%) changes the contour position by less than $0.2\ \mu\text{m}$. Thus the final accuracy Δ on the contour determination is limited by the quality of the image rather than by the algorithm. It is about $0.5\ \mu\text{m}$, over a sensor radius of about $15\ \mu\text{m}$.

Once the 3D contour of the sensor has been determined from the images, a renormalization factor $r = 0.935$ must be applied to the sensor's shape along the optical axis (z) direction. This factor takes into account a geometrical correction due to light refraction through the tissue/PDMS interface, which acts like a spherical diopter between two media of different optical indices ($1.35 < n_1 < 1.40$ for the living tissue; $n_2 \approx 1.44$ for PDMS). The factor r was calibrated *in situ*, by comparing the shape of hard non-deformable spherical sensors ($\mu \sim 2 \times 10^4$ Pa) to their reconstructed image. Calibrations were performed both in cell aggregates and in zebrafish embryos, leading to the same value $r = 0.935 \pm 0.02$, which was retained in the following.

With this active contour method, we estimate that we can detect a sensor deformation if the difference between two half axes is at least equal to threshold $\Delta = 0.5\ \mu\text{m}$, which represents the accuracy of our measurements.

Results

Sensors mechanical calibration

As shown in section **Strain-stress relationship**, determining *in situ* the local stress tensor requires to calibrate the sensors shear modulus μ. Its value was determined by two methods, first at the macroscopic scale with a commercial rheometer, and secondly *in situ* at the sensor's scale with a custom-made setup allowing uniaxial compression of aggregates.

Macroscopic rheometry

A rheometer (ARES G2) was used to follow the evolution of the elastic moduli of the PDMS preparation during its gelification. The polymerizable mixture was introduced in either plate-plate or cone-plate geometry, and maintained at a constant temperature $T = 60^\circ\text{C}$ or $T = 80^\circ\text{C}$, whilst the storage and loss moduli G' and G'' were measured every $15\ \text{min}$, in the range $0.1\ \text{hz} < f < 10\ \text{hz}$. A typical gelification curve is shown in Figure S2: after a transient increase during about one hour, G' gradually tends towards a plateau, which final

value is reached after ~ 12 h at $T = 60\,^{\circ}$C, or ~ 3 h at $T = 80\,^{\circ}$C. The same behavior is observed for G''.

At any given stage of gelification, G' was found independent of the excitation frequency f, and G'' increased approximately linearly with f, which corresponds to a Kelvin-Voigt behavior. Moreover, at the end of the gelification plateau, the ratio G'/G'' was found of the order of 10 at $f = 10$ hz for a standard gel composition. Thus, when the PDMS gel is submitted to a static (or very slowly varying) stress, it may be considered as a purely elastic solid, and it is legitimate to confound its static shear modulus μ with its storage modulus G' extrapolated at $f = 0$ hz.

At the end of the polymerization plateau, G' does not evolve any more, and its value is retained in the following as the value of the shear modulus μ_b for bulk polymerized PDMS. This value strongly depends on the mixture composition. It is close to 500 Pa for $m_{cross} = 0.0160\ m_{DMS}$, but reaches 1000 Pa for $m_{cross} = 0.0170\ m_{DMS}$. We noticed that the final value of μ_b depends also, but in a lesser extent, on the crosslinker and inhibitor concentrations, and on the temperature set for gelification. However, once fully polymerized, the shear modulus μ_b of the elastomer remains constant and does not depend on the operating temperature.

To compare the shear modulus μ_d of small spherical sensors to the one of bulk PDMS μ_b, we used a dispersion of the polymerizable mixture in water: a small amount of this mixture was added to water and vigorously shaken for a few seconds to makea coarse emulsion. The suspension was left to buoy up at room temperature, during a timelapse τ, and centrifugated until complete droplets coalescence. The supernatent was then sampled, and baked in the rheometer in the same conditions as bulk PDMS,i.e. at $T = 80\,^{\circ}$C during ~ 3 h. The evolution of G' during polymerization was similar to the one of the bulk, but the final plateau value μ_d was always found smaller that the bulk value μ_b measured for the non-emulsified mix having the same composition . The ratio μ_d / μ_b reached a stable plateau value ≈ 0.43 when $\tau \gtrsim 24$ h. We interpreted this observation by assuming that a small amount of a mix component, likely the crosslinker, may diffuse out of the DMS emulsion droplets and dissolve in the surrounding water. As seen above, a small variation of the crosslinker concentration is enough to induce a significant change in the final mechanical properties of the gel. Since the microsensors are made from small droplets suspended in water before polymerization, this effect has to be considered for a proper calibration of their mechanical properties. In practice, we decided to measure μ_b with the rheometer for every batch of bulk mix polymer used to make microsensors, and then to apply a constant corrective factor in order to get an estimate of the final shear modulus μ_d of the spherical elastic sensors: $\mu_d = 0.43\ \mu_b$.

In situ calibration in aggregates

At the microsensor's length scale, one expects that capillary effects, due to the non-zero surface tension $\gamma_c \sim 10$ mN/m between the tissue and the PDMS sensor of radius $a \sim 15\ \mu$m, might affect its global mechanical response (Style et al., 2017; Bico et al., 2018). Indeed, the contribution of the Laplace term $\frac{\gamma_c}{a} \sim 650$ Pa is comparable to the macroscopic

shear modulus μ_d of the PDMS dispersion. This means that the relationship between the applied external stress and the deformation of the sensor involves both the shear stress modulus μ_d and the surface tension γ_c. For small deformations, it has been shown that one can take into account this elasto-capillary contribution by introducing an effective elastic constant μ_e (Carbonaro et al., 2020):

$$\bar{\bar{\sigma}}^d = 2\mu_e \bar{\bar{\varepsilon}} \tag{9}$$

with

$$\mu_e = \mu_d + K\frac{\gamma_c}{a} \tag{10}$$

K is a dimensionless constant of order unity. We thus performed an *in situ* calibration on a sensor embedded in a tissue, in order to directly measure μ_e.

For this calibration, we used a custom-made uniaxial rheometer, allowing to apply either a controlled force, or a controlled deformation to a cell aggregate (Desprat et al., 2005; 2006; Mitrossilis et al., 2010). To summarize, the cell aggregate may be squeezed between two glass plates, a rigid one and a flexible one acting like a cantilever. The plates are actuated by two piezoelectric stages. A feedback loop maintains the extremity of the flexible plate, on the aggregate side, at a fixed position, whileits other extremity is free to relax with time. This allows to record the evolution of the force $F(t)$ exerted on the aggregate, at constant aggregate's deformation. $F(t)$ is calculated from the flexible plate's deflection, knowing its rigidity $k = 81.2\ nN/\mu m$.

Practically, we selected a CT26 aggregate of diameter comprised between 100 and $200\ \mu m$, containing a sensor localized close to the aggregate center, and we seized it between the two plates of the rheometer (Figure 4a). We then applied a step motion to the rigid plate to squeeze the aggregate, while the flexible plate extremity close to the aggregate was regulated at constant position. From this initial instant we recorded the relaxation of the flexible plate's deflection during 15 to 30 min, and thus the time evolution $F(t)$, while the aggregate deformation remained constant. Simultaneously, we imaged the shape of the sensor in its median plane (Figure 4b). Two or three successive squeezings and relaxations were operated on the same aggregate. From these relaxations we inferred at any time t the force $F(t)$ exerted on the aggregate, and the deformations $\varepsilon_{zz}(t)$ and $\varepsilon_{rr}(t)$ of the sensor, respectively in the compression direction and perpendicular to it.

As detailed in the appendix, we developed a model to establish the relationship between the sensor's deformation $\bar{\bar{\varepsilon}}$, and the average stress in the equatorial plane of the aggregate, defined as:

$$\sigma_a(t) = \frac{F(t)}{\pi R_1^2} \tag{11}$$

This model predicts:

$$\sigma_a = -\frac{3\mu_e}{1+\frac{R_1}{2R_2}}\varepsilon_{zz} + \gamma_{ag}\left(\frac{1}{R_2}-\frac{1}{R_1}\right)$$
$$= \frac{3\mu_e}{1+\frac{R_1}{2R_2}}2\varepsilon_{rr} + \gamma_{ag}\left(\frac{1}{R_2}-\frac{1}{R_1}\right) \quad (12)$$

Here R_1 represents the equatorial radius of the aggregate, R_2 its curvature radius in the observation plane (Fig. 4b_1), and γ_{ag} is the surface tension between the aggregate and the culture medium (not to be confused with the sensor/aggregate surface tension γ_c). Eq. (12) is valid under the following approximations: (i) the aggregate is supposed spherical at rest and the z axis is a cylindrical symmetry axis at any time; (ii) the sensor does not perturbate the stress distribution in the aggregate; (iii) the sensor is approximately at the center of the aggregate; (iv) the component $\sigma_{zz}(t)$ is assumed to be homogeneous in any plane perpendicular to the main compression axis.

Figure S3 shows an example of the time evolution of $\sigma_a(t), \varepsilon_{zz}(t)$ and $\varepsilon_{rr}(t)$, immediately after a compression step on an aggregate. Figure 4c reports the relationship between the sensor deformations $\varepsilon_{zz}(t), \varepsilon_{rr}(t)$ and the average stress $\sigma_a(t)$ for the same set of data. During the first 30 s, both the average stress and the sensor deformation relax rapidly with time (yellow points on Figure S2 and Figure 4c). It is likely that this regime is dominated by rapid relaxation processes, such as cytoplasm viscoelasticity, intercellular adhesion remodelling and T1 processes, and that the stress components are heterogeneous in the aggregate during this timelapse. On the other hand, at longer time, the relaxation slows down and one expects that hypothesis (iv) of our model, namely in plane spatial homogeneity of σ_{zz}, becomes verified. In this regime (red and blue points on Figure S2 and Figure 4c), $igma_a(t)$ linearly varies with $\varepsilon_{zz}(t)$, according to the model prediction given by Eq. (12) . Hence, from the linear fits shown in figure 4c, one can extract the values of the effective shear modulus $\mu_e = 790 \pm 160$ Pa and of the aggregate surface tension $\gamma_{ag} = 9 \pm 2$ mN/m for this particular experiment. Note that we experimentally measure $\varepsilon_{zz} \approx -2\varepsilon_{rr}$ at any time, which is consistent with the sensor's incompressibility and with the cylindrical symmetry assumptions.

Two gels of slightly different compositions have been tested. Within our experimental accuracy, no significant difference can be detected between the value of $\bar{\mu}_e$, averaged over N assays in different aggregates, and the value of μ_d measured at the macroscopic scale for a coarse emulsion made out of the same gel (see Table 1). These results do not allow us to isolate the contribution of capillary effects in the effective shear modulus μ_e, according to Eq. 10. Either this contribution is smaller than expected, or the determination of μ_d and μ_e is not accurate enough to measure the difference between them. In the following, we will take μ_d as the reference value for the effective elastic shear modulus of the sensors.

From the uniaxial compression of aggregates we can also infer the surface tension γ_{ag} between the aggregate and the culture medium. The values range from 3 to $12\ \mathrm{mN/m}$ for different aggregates. Although the dispersion is important, the order of magnitude corresponds to the expected one.

Stress distribution in cell aggregates

13 aggregates, containing deformable sensors located at different positions, were imaged with a 2-photon microscope. We analysed the shape of 17 sensors. To compare the results, we define a dimensionless position $r = r_c / R_a$ as the ratio of the distance r_c from the aggregate center to the sensor center, over the distance R_a from the aggregate center to the aggregate edge in the direction of the sensor. This definition takes into account the fact that the aggregate might be not spherical but slightly ellipsoidal.

The results are gathered in Fig. 5a. Each sensor is set at its reduced position r, and is represented by an ellipse showing its deformation projected in the (x, y) plane of the image. Since the actual deformations are small ($<10\%$), they were multiplied by a factor 4 on the scheme to be visible. The main components of the associated shear stress are represented as red bars of length proportional to the stress amplitude. In most cases, one of the main axes remains close to the Oz optical axis, which justifies the projection in the (x, y) plane.

By looking at the stress orientation and amplitude, one retrieves several pieces of information:

First, the in-plane main axes of the sensors are mostly aligned along the radial and orthoradial directions of the aggregate referential. Fig. 5b represents the distribution of angles between the radial direction and the sensor'slonger axis direction (blue: sensors showing a difference in half axes larger than the estimated accuracy threshold $0.5\ \mu\mathrm{m}$; red: other sensors). This distribution is non-uniform and indicates that the sensors are principally compressed in the orthoradial direction.

Second, the component σ_{zz}, represented by a color code in Fig. 5a, is always positive and ranges between 0 and 250 Pa (see **Discussion**).

Third, the stress amplitude $\|\boldsymbol{\sigma}\|$ varies from the center to the edge of the aggregate. $\|\boldsymbol{\sigma}\|$ is defined as the norm of the stress deviator:

$$\|\boldsymbol{\sigma}\| = \left(\left(\sigma^{d}_{XX}\right)^2 + \left(\sigma^{d}_{YY}\right)^2 + \left(\sigma^{d}_{ZZ}\right)^2 \right)^{1/2} \tag{13}$$

The histogram of $\|\boldsymbol{\sigma}\|$ is represented in Fig. 5c versus the normalized distance r. Despite the uncertainty, we observe a significant trend for $\|\boldsymbol{\sigma}\|$ to increase with r. Given the accuracy of our measurements, the maximum of $\|\boldsymbol{\sigma}\|$ seen in Fig. 5c might not be significant. More data would be necessary to improve the statistics.

In principle the evolution of this stress map can be followed in time. We were able to image the spreading of some aggregates deposited on the bottom plate of the Petri dish, during a few hours, by taking stacks every 15 min. In most cases, the axes orientations and half-lengths of the sensors remained stable with time, within experimental accuracy. Longer recordings would be necessary to see an evolution, and to follow the aggregate spreading process until its term.

Stress distribution in the prechordal plate of zebrafish embryos

In vivo, the spatial distribution of mechanical stresses, their inhomogeneities and their local anisotropy play a determinant role in the morphogenesis process, since they directly influence cell polarization and migration. For instance, it was established *in vitro* that Xenopus prechordal plate cells can be polarized by application of a mechanical stress of a few Pa (Weber et al., 2012). The prechordal plate (PPl) is a group of cells, that are the first ones to internalize on the dorsal side of the embryo, at the onset of gastrulation. During gastrulation, they migrate in direction of the animal pole, followed by notochord precursors (Kimmel et al., 1995; Solnica-Krezel et al., 1995). Based on this observation, it was proposed that migration of the PPl is guided *in vivo* by the existence of stress anisotropies within the tissue, used by cells as directional cues (Weber et al., 2012; Behrndt and Heisenberg, 2012). Our sensors are well suited to measure the 3D stress anisotropy andto map the stress in the PPl. Conversely, the PPl appeared as a good model to demonstrate their *in vivo* capabilities.

The prechordal plate and the notochord cells are labelled in the *Tg(gsc:GFP)* line, which was used in these experiments. Sensors were implanted in the PPl of seven different embryos. As an example, Fig. S4 shows a mesoscale view of the PPl containing a sensor, and enlarged images on the same sensor presenting a visible deformation. Some sensors could be followed over time, by taking images every 30 s or 60 s. An overview of the full dataset is shown in Supporting Information, Figure S5. We report here a selection of 12 measurements, at different stages of gastrulation, from 60 to 85% of epiboly. The common effective shear modulus of all the sensors was $\mu_d = 430$ Pa. To analyze the stress spatial distribution, the PPl was divided into 9 zones (front/middle/rear and left/center/right), as shown in figure 6e. For legibility, the projection of the shear stresses in the PPl (x, y) plane is drawn as an ellipse for each sensor, while the projection along the perpendicular axis z (confounded with the observation axis) is represented by a color code. In the PPl plane, x is the direction of the PPl progression and y the perpendicular one. All the stress components lie in a range comprised between $+60$ and -60 Pa, with approximately equal distribution between positive and negative values.

From figure 6e, no evident correlation emerges between the sensor location in one of the 9 zones of the PPl and the stress orientation and amplitude in the same zone. However, in Fig. 6f, the value of the shear stress amplitude $\|\boldsymbol{\sigma}\|$, averaged over the left/center/right zones and over the different epiboly stages, is compared at the front ($N = 3$) and at the middle ($N = 7$) of the plate. The difference is significant and is a first indication that stress gradients exist in the PPl.

Concerning the time evolution of the stress, we were able to follow the stress components for 7 sensors, during 15 to 30 min, at different stages of epiboly. They did not show any significant changes, except for one event which we describe in detail in Supporting Information, Fig S6 and S7.

Discussion

In both experiments, *in vitro* and *in vivo*, we have demonstrated that our pipeline of techniques, based on the use of PDMS elastic microsensors embedded in living tissues, can be used to locally determine the amplitudes and orientations of the shear stress components, to map them across the tissue, and to retrieve their temporal evolution.

In vitro, for freely spreading cell aggregates, the order of magnitude of the shear stress amplitude typically lies between 10 and 100 Pa, consistently with other measurements in similar systems (Lucio et al., 2017; Lee et al., 2019; Mohagheghian et al., 2018). Moreover, Fig. 5c shows that the deviator stress amplitude σ increases from the aggregate center to its edge, and that the stress component along the orthoradial direction is larger than along the radial one. On the other hand, according to our observations, the optical axis Oz systematically coincides with one of the main shear stress axis, with a positive value of the shear (extension). A possible explanation would be that, besides the applied geometrical correction due to light refraction, light diffusion in the tissue may also affect the quality of the image, especially at large depth inside the tissue ($\gtrsim 100\ \mu\mathrm{m}$). If this is the case, the systematic elongation of the sensor in the z direction could be an artefact related to the imaging method. Fortunately, this does not affect our conclusions concerning the radial/orthoradial privileged orientations in the (x, y) plane, nor the variations of the stress amplitudewith reduced distance r.

It is interesting to compare these results with those reported in the literature. In the pioneering work by (Delarue et al., 2014a), after submitting reconstituted cell aggregates to an external pressure, it is observed that the cell density increases from the aggregate periphery to its center. The model developed in that paper attempts to correlate this density increase to the local cell polarization: the cell elongation evolves, on average, from the radial direction near the center to the orthoradialdirection close to the aggregate boundary. Actually, this differs from our own observations: our sensors are mainly oriented in the radial direction at the aggregate periphery, and the cell polarization is expected to be in the same direction, following the stress anisotropy. Besides the fact that the cell lines are different in the two experiments (BC52 *vs* CT26), one should keep in mind that an important external pressure is intentionally applied in Delarue et al. (2014a) in order to modify theaggregate organization and the cell growth conditions.

In another paper (Lee et al., 2019), hydrogel sensors are embedded in spherical aggregates made of HS-5 fibroblasts. In this paper two components of the full stress tensor $\bar{\bar{\sigma}}$ were measured *vs* the distance to the aggregate center, respectively in the radial and orthoradial directions in the observation plane. Both their amplitudes are comprised between -400 and -1500 Pa. Their average value represents the isotropic part of the stress: it is negative and thus corresponds to a compression. The difference between the two components, which is the local shear stress, is of the order of ± 100 Pa, comparable to their measurements accuracy. This order of magnitude is similar to ours. Moreover, they observe that both stress components increase from the aggregate edge, to reach a maximum value, and then decrease again towards the aggregate center. Although the two experiments give access to different quantities (total stress in their case, shear stress in ours), the behaviors observed in both situations are consistent.

In vivo, in the prechordal plate of the Zebrafish embryo, we were able to measure both the amplitude and orientation of the main stress components at different stages of epiboly. The retrieved values are of the expected order of magnitude, 10^2 Pa, and the sensitivity is of order of 10^1 Pa. The shear stress amplitude appears larger at the center of the PPl than at its front, which supports the hypothesis that stress gradientsexist in the PPl and might play an active role in the PPl migration. A systematic survey of the stress amplitude and orientation in the different PPl regions is needed to confirm this hypothesis. Concerning time evolution, we could follow the stresses only on a short time interval as compared to the gastrulation characteristic time. This might explain why we observed only one event exhibiting a measurable time evolution. Similar events have to be identified before discussing their possible relevance in the full migration process. Another important issue, which was not

investigated here, concerns the stress distribution in the direction orthogonal to the PPl plane. Indeed, one suspects that the friction of the PPl over the neurectoderm might play an important role in the migration process (Smutny et al., 2017). Thus, further investigations will also have to include the vertical position of the sensor inside the PPl as one of the relevant parameters of the problem.
To conclude, we have assembled a pipeline of techniques which meets all the requirements to quantitatively map in 3D and in real time the local shear stresses in living tissues, with a sensitivity of order of 10 Pa. In complement to existing techniques, it appears as a valuable tool to investigate the role of mechanical constraints in morphogenesis and development.

Acknowledgements
We acknowledge Alain Richert, Gaëtan Mary, Magid Badaoui, Alain Ponton and Sandra Lerouge for their assistance and advices in experimental handling, Héléne Delanoé-Ayari for critical reading of the manuscript, and Mathieu Roché and Julien Dervaux for fruitful discussions. We acknowledge the ImagoSeine facility, at Institut Jacques Monod, especially Xavier Baudin and Orestis Faklaris, and the Polytechnique Bioimaging Facility, for assistance with live imaging on their equipments.

Competing interests
The authors declare no competing interests.

Contribution
A.S, F. Gr. and F. Ga. designed the experiments, with the help of G.C., A.A., A.B, N.D.; A.S. carried out the experiments and data analysis, together with A.B. for the Zebrafish part under the supervision of N. D.; G.C. supervised the chemistry of fluorescent labelling; A.A. conducted the uniaxial rheometry; F. Ga. did the appendix calculations; C.N. inspired the scientific process and methodology; F. Gr. and F. Ga. supervised the work; A.S, F. Gr. and F. Ga. wrote the manuscript. All authors have read,corrected and approved the manuscript.

Funding
This work was made possible through a fellowship of the Ecole Doctorale EDPIF (AS), and a grant from the Domaine d'Intéret Majeur program (complex systems) of the Ile-de-France region. Part of it was also supported by the labex <<Who Am I?>>, labex ANR-11-LABX-0071, and the Université de Paris, Idex ANR-18-IDEX-0001 funded by the French Government through its <<Investments for the Future>> program. The ImagoSeine facility is a member of the France BioImaging infrastructure and is supported by Agence Nationale de la Recherche (ANR-10-INSB-04). The Polytechnique Bioimaging Facility is partly supported by Région Ile-de-France (interDIM) and Agence Nationale de la Recherche (ANR-11-EQPX-0029 Morphoscope2, ANR-10-INBS-04 France BioImaging)

Data availability
The python code used for active contour detection is available here:
https://github.com/scikit-image/scikit-image/blob/main/skimage/segmentation/morphsnakes.py.

An example of contour determination can be found here:
https://github.com/Alex-code-lab/3D_contour_detection_and_fit_by_an_ellipsoid.

5. Appendix: Expression of the local stresses in an aggregate submitted to an uniaxial compression

In this section we describe a model to calculate all the components of the stress tensor at any point of an aggregate submitted to an uniaxial compression, from which we derive the expression of the deformation of an elastic incompressible sensor embedded in the aggregate.

Notations

We assume that the aggregate, initially spherical, is squeezed between two plates applying on it a force $\vec{F} = -F\vec{e}_z$, and that the problem respects the cylindrical symmetry around axis Oz. The notations are explicited in Fig. 7. We use cylindrical coordinates $M(r,\phi,z)$, O is the aggregate center. $R(z)$ is the radius of the curve generating the aggregate cylindrical surface. The principal radii of curvature are:

$$R_\perp = \frac{R}{\cos\theta}$$

$$R_{\square} = -\frac{1}{\sin\theta}\frac{dR}{d\theta} \tag{14}$$

with $\tan\theta = -\frac{dR}{dz}$.

In the particular case of a circular profile, which is a non-necessary but sufficient approximation for most situations, one has:

$$\begin{aligned} R_{\square} &= cst = R_2 \\ R(z) &= R_1 - R_2 + R_2\cos\theta \\ \frac{1}{R_\perp} &= \frac{\cos\theta}{R(z)} = \frac{1}{R_2} - \frac{1}{R(z)}\left(\frac{R_1}{R_2} - 1\right) \end{aligned} \tag{15}$$

where R_1 is the equatorial radius.

The local stress tensor is written as:

$$\overline{\overline{\sigma}} = \begin{pmatrix} \sigma_{rr} & \sigma_{r\phi} & \sigma_{rz} \\ \sigma_{r\phi} & \sigma_{\phi\phi} & \sigma_{\phi z} \\ \sigma_{rz} & \sigma_{\phi z} & \sigma_{zz} \end{pmatrix} \tag{16}$$

Mechanical equilibrium

In the absence of external volumic force, the mechanical equilibrium condition is written: $\overrightarrow{\mathrm{div}}\left(\bar{\bar{\sigma}}\right) = \vec{0}$, *i.e.* in cylindrical coordinates:

$$\begin{aligned}
&\frac{\partial \sigma_{rr}}{\partial r} + \frac{1}{r}\frac{\partial \sigma_{r\phi}}{\partial \phi} + \frac{1}{r}\left(\sigma_{rr} - \sigma_{\phi\phi}\right) + \frac{\partial \sigma_{rz}}{\partial z} = 0 \\
&\frac{\partial \sigma_{r\phi}}{\partial r} + \frac{2}{r}\sigma_{r\phi} + \frac{1}{r}\frac{\partial \sigma_{\phi\phi}}{\partial \phi} + \frac{\partial \sigma_{\phi z}}{\partial z} = 0 \\
&\frac{\partial \sigma_{rz}}{\partial r} + \frac{1}{r}\sigma_{rz} + \frac{1}{r}\frac{\partial \sigma_{\phi z}}{\partial \phi} + \frac{\partial \sigma_{zz}}{\partial z} = 0
\end{aligned} \tag{17}$$

Due to the cylindrical symmetry, all the stress components are independent on the azimutal angle ϕ. Furthermore $\sigma_{r\phi} = \sigma_{z\phi} = 0$. Thus the above equations simplify into:

$$\begin{aligned}
&\frac{\partial \sigma_{rr}}{\partial r} + \frac{1}{r}\left(\sigma_{rr} - \sigma_{\phi\phi}\right) + \frac{\partial \sigma_{rz}}{\partial z} = 0 \\
&\frac{\partial \sigma_{rz}}{\partial r} + \frac{1}{r}\sigma_{rz} + \frac{\partial \sigma_{zz}}{\partial z} = 0
\end{aligned} \tag{18}$$

We can also write the mechanical equilibrium condition at the aggregate surface, *i.e.* for $r = R(z)$. By equilibrating the local stresses at the boundary with the external pressure p_a outside the aggregate and the Laplace pressure, one finds in projection along the r and z axes at any point $M(R,z)$ of the surface:

$$\sigma_{rr} + \sigma_{zr}\tan\theta = \sigma_{zz} + \frac{\sigma_{zr}}{\tan\theta} = -p_a - \gamma_{ag}\left(\frac{1}{R_{\perp}} + \frac{1}{R_{\parallel}}\right) \tag{19}$$

We recall that γ_{ag} represents the surface tension between the aggregate and the external medium.

Finally, following Norotte et al. (2008), the global balance of forces exerted on the aggregate, in a plane perpendicular to Oz, at coordinate z, can be expressed as:

$$\int \sigma_{zz} 2\pi r dr + 2\pi\gamma_{ag} R(z)\cos\theta = -F - \pi R^2 p_a \tag{20}$$

Expression of $\bar{\bar{\sigma}}(r,z)$

We assume in the following that the expressions of the components $\sigma_{zz}(r,z), \sigma_{rr}(r,z)$ and $\sigma_{\phi\phi}(r,z)$ can be approximated by a Taylor expansion to order r^2, according to:

$$\begin{aligned}\sigma_{zz}(r,z) &= -\sigma_0(z) + b_0(z)\,r^2 \\ \sigma_{rr}(r,z) &= -\sigma_1(z) + b_1(z)\,r^2 \\ \sigma_{\phi\phi}(r,z) &= -\sigma_2(z) + b_2(z)\,r^2\end{aligned} \tag{21}$$

The functions $\sigma_i(z)$ and $b_i(z)$ $(i = 0,1,2)$ account for the z-dependence of the stress components. As shown below, they can be explicitly calculated from Eqs. (18) to (20). Note that $\sigma_i(z)$ is positive in case of a compression.

From equation (18) one derives the expression of σ_{rz}:

$$\sigma_{rz}(r,z) = \frac{r}{2}\sigma_0'(z) - \frac{r^3}{4}b_0'(z) \tag{22}$$

where the prime stands for the z-derivative.

Introducing the expression of σ_{rz} (Eq.(22)) in Eq. (18) yields:

$$\begin{aligned}&2b_1(z)\,r + \frac{\sigma_2(z) - \sigma_1(z)}{r} + \left(b_1(z) - b_2(z)\right)r \\ &+ \frac{r}{2}\sigma_0''(z) - \frac{r^3}{4}b_0''(z) = 0\end{aligned} \tag{23}$$

Since the components of $\overline{\overline{\sigma}}$ must not diverge in $r = 0$, necessarily $\sigma_2(z) = \sigma_1(z)$. There remains:

$$3b_1(z) - b_2(z) + \frac{\sigma_0''(z)}{2} = \frac{r^2}{4}b_0''(z)$$

Because we limit the Taylor development to order r^2 for σ_{rr} and $\sigma_{\phi\phi}$, b_1 and b_2 do not depend on r. Consequently $b_0''(z) = 0$ and thus $b_0(z) = Az + B$, where A and B are two constants. Moreover, by z to $-z$ symmetry, σ_{zz} must be an even function of z, which implies $A = 0$. Therefore:

$$b_0(z) = B \tag{24}$$

Here B is a constant independent of z, but it may depend on time t if the stresses in the aggregate evolve with time.

At this stage an additional relation between $b_1(z)$ and $b_2(z)$ is required to close the equation system (18) to (20) and complete the calculation. In the following, we will assume for simplicity that the stress projection in any plane orthogonal to Oz is isotropic, which means $\sigma_{rr}(r,z) = \sigma_{\phi\phi}(r,z)$ and thus $b_1(z) = b_2(z)$. This most simple hypothesis can be partially justified by geometrical arguments, related to the incompressibility of the material, which we will not develop here. Other assumptions remain possible, but we have checked, after

performing the whole calculation in different cases, that the result is not modified except for some minor numerical factors. Under this assumption,Eq. (23) simplifies into:

$$b_1(z) = b_2(z) = -\frac{\sigma_0''(z)}{4} \tag{25}$$

The integral of Eq. (20) may be calculated using Eq. (21), which leads to:

$$\sigma_0(z) = p_a + \frac{F}{\pi R^2(z)} + \frac{2\gamma_{ag}\cos\theta(z)}{R(z)} + \frac{1}{2}BR^2(z) \tag{26}$$

Eqs. (24), (25) and (26) are sufficient to calculate all the components of the stress tensor, at any point of a cylindrical aggregate of generator $R(z)$. For instance, one finds for $\sigma_{zz}(r,z)$:

$$\sigma_{zz}(r,z) = -p_a - \frac{F}{\pi R^2(z)} - \frac{2\gamma_{ag}\cos\theta(z)}{R(z)} - \frac{1}{2}BR^2(z) + Br^2 \tag{27}$$

The only remaining free parameter in Eq. (27) is the constant B, the value of which will be discussed at the end of this section.

The other components $\sigma_{zr}(r,z)$ and $\sigma_{rr}(r,z) = \sigma_{\phi\phi}(r,z)$ can also be written after some long but straightforward calculations, using Eqs. (21), (22) and the boundary condition Eq. (19) to calculate $\sigma_1(z)$.

In the following, we only focus on the case of an aggregate with a circular profile, *i.e.* $R_{\perp} = R_2 = cst$, and we write down the stress components in its equatorial plane $z = 0$. In this plane, $R_{\perp} = R_1$ and $\theta = 0$, which leads to:

$$\sigma_{zz}(r,0) = -p_a - \frac{F}{\pi R_1^2} - \frac{2\gamma_{ag}}{R_1} + \frac{1}{2}BR_1^2 - BR_1^2\left(1 - \frac{r^2}{R_1^2}\right) \tag{28}$$

$$\sigma_{rr}(r,0) = \sigma_{\phi\phi}(r,0) = -p_a - \gamma_{ag}\left(\frac{1}{R_1} + \frac{1}{R_2}\right) \ldots + \frac{R_1}{R_2}\left[\frac{F}{2\pi R_1^2} - \frac{\gamma_{ag}}{2}\left(\frac{1}{R_2} - \frac{1}{R_1}\right) - \frac{BR_1^2}{4}\right]\left(1 - \frac{r^2}{R_1^2}\right) \tag{29}$$

$$\sigma_{rz}(r,0) = 0 \tag{30}$$

4. Deformation of a sensor embedded in the aggregate

We consider an elastic incompressible sensor, spherical at rest, embedded in the aggregate, of effective shear modulus μ_e. We assume that the mechanical properties of the sensor and of the aggregate are similar, and that the sensor diameter is small compared to the aggregate's one, so that the sensor inclusion does not perturbate the stress distribution in the aggregate. Due to incompressibility, only shear deformations of the sensor are admitted, and the strain-stress tensors relationship reduces to (see Eq. (2)):

$$2\mu_e \bar{\bar{\varepsilon}} = \bar{\bar{\sigma}}^d = \bar{\bar{\sigma}} - \frac{1}{3} tr\left(\bar{\bar{\sigma}}\right) \boldsymbol{I} \tag{31}$$

In the following, we assume that the stress is homogeneous over the sensor size. We also assume for simplicity that it is located in the equatorial plane $z = 0$, although the calculations could in principle be performed for any position in the aggregate. We introduce $\sigma_a = \frac{F}{\pi R_1^2}$ as the average stress exerted by the force F on the equatorial plane. Using Eqs. (28) and (29), one finds:

$$\sigma_a = -\frac{3\mu_e \varepsilon_{zz}(r)}{1 + \frac{R_1}{2R_2}\left(1 - \frac{r^2}{R_1^2}\right)} + \gamma_{ag}\left(\frac{1}{R_2} - \frac{1}{R_1}\right) + \frac{BR_1^2}{2}\left[\frac{2R_2 + (R_1 - 4R_2)\left(1 - \frac{r^2}{R_1^2}\right)}{2R_2 + R_1\left(1 - \frac{r^2}{R_1^2}\right)}\right] \tag{32}$$

Equivalently, in Eq. (32) one can replace $-\varepsilon_{zz}$ by $+2\varepsilon_{rr}$, since incompressibility implies $\varepsilon_{rr} = \varepsilon_{\phi\phi} = -\frac{\varepsilon_{zz}}{2}$.

At the aggregate center ($r = 0,\ z = 0$), Eq. (32) simplifies into:

$$\sigma_a = -\frac{3\mu_e \varepsilon_{zz}(r = 0)}{1 + \frac{R_1}{2R_2}} + \gamma_{ag}\left(\frac{1}{R_2} - \frac{1}{R_1}\right) + \frac{BR_1^2}{2}\left(\frac{R_1 - 2R_2}{R_1 + 2R_2}\right) \tag{33}$$

At the aggregate edge ($r = R_1,\ z = 0$), one has:

$$\sigma_a = -3\mu_e \varepsilon_{zz}(r = R_1) + \gamma_{ag}\left(\frac{1}{R_2} - \frac{1}{R_1}\right) + \frac{BR_1^2}{2} \tag{34}$$

Choice of the value of B

In this model, B has a homogeneous value over the volume of the sensor, but it may vary over time. Indeed, in the experiment one applies to the rigid plate at $t = 0$ a displacement step, which imprints a constant deformation to the aggregate. Immediately after the step, the stress in the aggregate is inhomogeneous, but it rapidly evolves, within a few minutes,

through different relaxation mechanisms, to become homogeneous again at the end of relaxation. $B(t)$ is therefore a function of time which must relax towards zero at infinite time. To interpret our data concerning $\sigma_a(\varepsilon)$, we discard the first instants of the relaxation, and we only consider the long time limit, for which we expect the stresses to be homogeneous again, allowing usto make the approximation $B = 0$. Within this assumption, Eq. (33) exactly reduces to Eq. (12) used in the main text. To comfort this assumption, we also performed the data analysis by taking a non-zero value for B, leading to parabolic variations for σ_{zz} as a function of r. Assuming for instance that σ_{zz} vanishes at the aggregate edge ($r = R_1,\ z = 0$), from Fig. (4c) one retrieves $\mu_e = 670$ Pa, instead of $\mu_e = 790$ Pa in the case $B = 0$. Considering all other sources of uncertainty, the results do not appear significantly different.

References

Angeli, S. and Stylianopoulos, T. (2016). Biphasic modeling of brain tumor biomechanics and response to radiation treatment. *Journal of Biomechanics* **49**, 1524-1531.

Bambardekar, K., Clément, R., Blanc, O., Chardés, C. and Lenne, P.-F. (2015). Direct laser manipulation reveals the mechanics of cell contacts in vivo. *Proceedings of the National Academy of Sciences* **112**, 1416-1421.

Behrndt, M. and Heisenberg, C.-P. (2012). Spurred by resistance: Mechanosensation in collective migration. *Developmental Cell* **22**, 3–4.

Bendaoud, M. (2017). *Développement de méthodes d'extraction de contours sur des images à niveaux de gris*. Ph.D. thesis.

Bico, J., Reyssat, t. and Roman, B. (2018). Elastocapillarity: When surface tension deforms elastic solids. *Annual Review of Fluid Mechanics* **50**, 629–659.

Bonnet, I., Marcq, P., Bosveld, F., Fetler, L., Bellaiche, Y. and Graner, F. (2012). Mechanical state, material properties and continuous description of an epithelial tissue. *Journal of The Royal Society Interface* **9**, 2614-2623.

Borghi, N., Sorokina, M., Shcherbakova, O., Weis, W., Pruitt, B., Nelson, W. and Dunn, A. (2012). E-cadherin is under constitutive actomyosin-generated tension that is increased at cell-cell contacts upon externally applied stretch. *Proceedings of the National Academy of Sciences* **109**, 12568-12573.

Boutillon, A., Giger, F. A. and David, N. B. (2018). *Analysis of In Vivo Cell Migration in Mosaic Zebrafish Embryos*. New York, NY: Springer New York, pages 213–226.

Brodland, G., Veldhuis, J., Kim, S., Perrone, M., Mashburn, D. and Hutson, M. S. (2014). Cellfit: A cellular force-inference toolkit using curvilinear cell boundaries. *PLoS ONE* **9**, 1–15.

Butt, H.-J., Cappella, B. and Kappl, M. (2005). Force measurements with the atomic force microscope: Technique, interpretation and applications. *Surface Science Reports* **59**, 1–152.

Campàs, O. (2016). A toolbox to explore the mechanics of living embryonic tissues. *Seminars in Cell and Developmental Biology* **55**, 119–130.

Campàs, O., Mammoto, T., Hasso, S., Sperling, R., O'Connell, D., Bischof, A. and Ingber, D. (2014). Quantifying cell-generated mechanical forces within living embryonic tissues. *Nature Methods* **11**, 183–189.

Carbonaro, A., Chagua-Encarnacion, K.-N., Charles, C.-A., Phou, T., Ligoure, C., Mora, S. and Truzzolillo, D. (2020). Spinning elastic beads: a route for simultaneous measurements of the shear modulus and the interfacial energy of soft materials. *Soft Matter* **16**, 8412–8421.

Caselles, V., Catte, F., Coll, B. and Dibos, F. (1993). A geometric model for edge detection. *Numerische Mathematik* **66**, 1–31.

Chiou, K., Hufnagel, L. and Shraiman, B. (2012). Mechanical stress inference for two dimensional cell arrays. *PLoS Computational Biology* **8**, 1–9.

Delarue, M., Joanny, J.-F., Jülicher, F. and Prost, J. (2014a). Stress distributions and cell flows in a growing cell aggregate. *Interface Focus* **4**, 20140033.

Delarue, M., Montel, F., Vignjevic, D., Prost, J., Joanny, J. and Cappello, G. (2014b). Compressive stress inhibits proliferation in tumor spheroids through a volume limitation. *Biophysical Journal* **107**, 1821–1828.

Desprat, N., Guiroy, A. and Asnacios, A. (2006). Microplates-based rheometer for a single living cell. *Reviex of scientifc intruments* **77**, 055111.

Desprat, N., Richert, A., Simeon, J. and Asnacios, A. (2005). Creep function of a single living cell. *Biophysical Journal* **88**, 2224-2233.

Desprat, N., Supatto, W., Pouille, P.-A., Beaurepaire, E. and Farge, E. (2008). Tissue deformation modulates twist expression to determine anterior midgut differentiation in drosophila embryos. *Developmental Cell* **15**, 470–477.

Doitsidou, M., Reichman-Fried, M., Stebler, J., Köprunner, M., Dorries, J., Meyer, D., Esguerra, C., Leung, T. and Raz, E. (2002). Guidance of primordial germ cell migration by the chemokine sdf-1. *Cell* **11**, 647–659.

Dolega, M., Delarue, M., Ingremeau, F., Prost, J., Delon, A. and Cappello, G. (2017). Cell-like pressure sensors reveal increase of mechanical stress towards the core of multicellular spheroids under compression. *Nature Communications* **8**, 14056.

Elkin, B., Azeloglu, E., Costa, K. and Morrison III, B. (2007). Mechanical heterogeneity of the rat hippocampus measured by atomic force microscope indentation. *Journal of Neurotrauma* **24**, 812-822.

Franze, K. (2011). Atomic force microscopy and its contribution to understanding the development of the nervous system. *Current Opinion in Genetics and Development* **21**, 530-537.

Gomez-Gonzalez, M., Latorre, E., Arroyo, M. and Trepat, X. (2020). Measuring mechanical stress in living tissues. *Nature Reviews Physics* **2**, 300–317.

Grashoff, C., Hoffman, B., Brenner, M., Zhou, R., Parsons, M., Yang, M. and Schwartz, M. (2010). Measuring mechanical tension across vinculin reveals regulation of focal adhesion dynamics. *Nature* **466**, 263–266.

Guevorkian, K., Colbert, M.-J., Durth, M., Dufour, S. and Brochard-Wyart, F. (2010). Aspiration of biological viscoelastic drops. *Physical Review Letters* **104**, 218101.

Guirao, B., Rigaud, S. U., Bosveld, F., Bailles, A., Lopez-Gay, J., Ishihara, S., Sugimura, K., Graner, F. and Bellaiche, Y. (2015). Unified quantitative characterization of epithelial tissue development. *eLife* **4**, e08519.

Haejune, K. (2007). Controlled production of emulsion drops using an electric field in a flow-focusing microfluidic device. *Applied Physics Letters* **91**, 211–218.

Hamada, H. (2015). Role of physical forces in embryonic development. *Seminars in Cell and Developmental Biology* **47-48**, 88–91.

Heisenberg, C. and Bellaïche, Y. (2013). Forces in tissue morphogenesis and patterning. *Cell* **153**, 948–962.

Helfrich, W. (1973). Elastic properties of lipid bilayers: theory and possible experiments. *Z Naturforsch* **28**, 693–703.

Herrera-Perez, R. and Karen, K. (2018). Biophysical control of the cell rearrangements and cell shape changes that build epithelial tissues. *Current Opinion in Genetics and Development* **51**, 88–95.

Hiramatsu, R., Matsuoka, T., Kimura-Yoshida, C., Han, S.-W., Mochida, K., Adachi, T. and Matsuo, I. (2013). External mechanical cues triggerthe establishment of the anterior-posterioraxis in early mouse embryos. *Developmental Cell* **27**, 131–144.

Hobbie, E. K., Lin-Gibson, S. and Kumar, S. (2008). Non-brownian microrheology of a fluid-gel interface. *Physical Review Letters* **100**, 076001.

Hochmuth, R. (2000). Micropipette aspiration of living cells. *Journal of Biomechanics* **44**, 15-22.

Hosu, B. G., Jakab, K., Bánki, P., Tóth, F. I. and Forgacs, G. (2003). Magnetic tweezers for intracellular applications. *Review of Scientific Instruments* **74**, 4158-4163.

Ishihara, S., Sugimura, K., Cox, S., Bonnet, I., Bellaïche, Y. and Graner, F. (2013). Comparative study of non-invasive force and stress inference methods in tissue. *The European Physical Journal E* **36**, 45.

Kass, M., Witkin, A. and Terzopoulos, D. (1988). Snakes: Active contour models. *International Journal of Computer Vision* **1**, 321–331.

Krieg, M., Arboleda-Estudillo, Y., Puech, P.-H., Käfer, J., Graner, F., Müller, D. and Heisenberg, C.-P. (2008). Tensile forces govern germ-layer organization in zebrafish. *Nature Cell biology* **10**, 429–436.

Landau, L., Lifshitz, E., Kosevich, A. and Pitaevskii, L. (1986). *Theory of Elasticity: course of theoretical physics*, volume 7. Elsevier.

Lau, K., Tao, H., Liu, H., Wen, J., Sturgeon, K., Sorfazlian, N. and Hopyan, S. (2015). Anisotropic stress orients remodelling of mammalian limb bud ectoderm. *Nature Cell Biology* **17**, 569-579.

Le Goff, L., Rouault, H. and Lecuit, T. (2013). A global pattern of mechanical stress polarizes cell divisions and cell shape in the growing drosophila wing disc. *Development* **140**, 4051–4059.

Lee, W., Kalashnikov, N., Mok, S., Halaoui, R., Kuzmin, E., Putnam, A. and Moraes, C. (2019). Dispersible hydrogel force sensors reveal patterns of solid mechanical stress in multicellular spheroid cultures. *Soft Matter* **13**, 4210–4213.

Lucio, A. A., Mongera, A., Shelton, E., Chen, R., Doyle, A. M. and Campas, O. (2017). Spatiotemporal variation of endogenous cell- generated stresses within 3D multicellular spheroids. *Scientific Reports* **7**, 12022.

Marquez-Neila, P., Baumela, L. and Alvarez, L. (2014). A morphological approach to curvature-based evolution of curves and surfaces. *IEEE Transactions on Pattern Analysis and Machine Intelligence* **36**, 2–17.

Mazuel, F., Reffay, M., Du, V., Bacri, J.-C., Rieu, J.-P. and Wilhelm, C. (2015). Magnetic flattening of stem-cell spheroids indicates a size-dependent elastocapillary transition. *Physical Review Letters* **114**, 1416-1421.

Mgharbel, A., Delanoë-Ayari, H. and Rieu, J. (2009). Measuring accurately liquid and tissue surface tension with a compression plate tensiometer. *HFSP Journal* **3**, 213-221.

Mitchison, J. and Swann, M. (1954). The mechanical properties of the cell surface: I. the cell elastimeter. *Journal of Experimental Biology* **31**, 443–460.

Mitrossilis, D., Fouchard, J., Guiroy, A., Desprat, N., Rodriguez, N., Fabry, B. and Asnacios, A. (2009). Single-cell response to stiffness exhibits muscle-like behavior. *Proceedings of the National Academy of Sciences* **106**, 18243-18248.

Mitrossilis, D., Fouchard, J., Pereira, D., Postic, F., Richert, A., Saint-Jean, M. and Asnacios, A. (2010). Real-time single-cell response to stiffness. *Proceedings of the National Academy of Sciences* **107**, 16518–16523.

Mohagheghian, E., Luo, J., Chen, J., Chaudhary, G., Chen, J., Sun, J. and Wang, N. (2018). Quantifying compressive forces between living cell layers and within tissues using elastic round microgels. *Nature Communications* **9**, 1878.

Mongera, A., Rowghanian, P., Gustafson, H., Shelton, E., Kealhofer, D., Carn, E. K. and Campàs, O. (2018). A fluid-to-solid jamming transition underlies vertebrate body axis elongation. *Nature* **561**, 401–405.

Monnier, S., Delarue, M., Brunel, B., Dolega, M., Delon, A. and Cappello, G. (2016). Effect of an osmotic stress on multicellular aggregates. *Methods* **94**, 114–119.

Neuman, K. C. and Nagy, A. (2008). Single-molecule force spectroscopy: optical tweezers, magnetic tweezers and atomic force microscopy. *Nature Methods* **5**, 491-505.

Nienhaus, U., Aegerter-Wilmsen, T. and Aegerter, C. M. (2009). Determination of mechanical stress distribution in drosophila wing discs using photoelasticity. *Mechanisms of Development* **126**, 942 – 949.

Nier, V., Jain, S., Lim, C. T., Ishihara, S., Ladoux, B. and Marcq, P. (2016). Inference of internal stress in a cell monolayer. *Biophysical Journal* **110**, 1625–1635.

Norotte, C., Marga, F., Neagu, A., Kosztin, I. and Forgacs, G. (2008). Experimental evaluation of apparent tissue surface tension based on the exact solution of the laplace equation. *Europhysics Letters* **81**, 46003.

Northcott, J. M., Dean, I. S., Mouw, J. K. and Weaver, V. M. (2018). Feeling stress: The mechanics of cancer progression and aggression. *Frontiers in Cell and Developmental Biology* **6**, 17.

Porazinski, S., Wang, H., Asaoka, Y., Behrndt, M., Miyamoto, T., Morita, H. and Furutani-Seiki, M. (2015). Yap is essential for tissue tension to ensure vertebrate 3d body shape. *Nature* **521**, 217-221.

Rauzi, M., Verant, P., Lecuit, T. and Lenne, P.-F. (2008). Nature and anisotropy of cortical forces orienting drosophila tissue morphogenesis. *Nature Cell Biology* **10**, 1401-1410.

Roca-Cusachs, P., Conte, V. and Trepat, X. (2017). Quantifying forces in cell biology. *Nature Cell Biology* **19**, 742-751.

Roffay, C., Chan, C.-J., Guirao, B., Hiiragi, T. and Graner, F. (2021). Inferring cell junction tension and pressure from cell geometry. *Develoment* **148**, 1–16.

Schluck, T. and Aegerter, C. M. (2010). Photo-elastic properties of the wing imaginal disc of Drosophila. *Eur. Phys. J. E* **33**, 111–115.

Schneider, M., Tran, Y. and Tabeling, P. (2011). Benzophenone absorption and diffusion in poly(dimethylsiloxane) and its role in graft photo-polymerization for surface modification. *Langmuir* **27**, 1232–1240.

Smutny, M., Akos, Z., Grigolon, S., Shamipour, S., Ruprecht, V., Capek, D., Behrndt, M., Papusheva, E., Tada, M., Hof, B., Vicsek, T., Salbreux, G. and Heisenberg, C.-P. (2017). Friction forces position the neural anlage. *Nature Cell Biology* **19**, 306.

Souchaud, A. (2020). *Cartographie des contraintes mécaniques in situ dans les tissus vivants*. Ph.D. thesis, Université de Paris.

Style, R. W., Jagota, A., Hui, C.-Y. and Dufresne, E. R. (2017). Elastocapillarity: Surface tension and the mechanics of soft solids. *Annual Review of Condensed Matter Physics* **8**, 99–118.

Sugimura, K., Lenne, P.-F. and Graner, F. (2016). Measuring forces and stresses in situ in living tissues. *Development* **143**, 186–196.

Tanase, M., Biais, N. and Sheetz, M. (2007). Magnetic tweezers in cell biology. *Cell Mechanics* **22**, 473-493.

Tinevez, J.-Y., Schulze, U., Salbreux, G., Roensch, J., Joanny, J.-F. and Paluch, E. (2009). Role of cortical tension in bleb growth. *Proceedings of the National Academy of Sciences* **106**, 18581-18586.

Toworfe, G., Adams, C., Shapiro, I. and Ducheyne, P. (2004). Fibronectin adsorption on surface-activated poly(dimethylsiloxane) and its effect on cellular function. *Journal of biomedical materials research. Part A* **71**, 449–61.

Träber, N., Uhlmann, K., Girardo, S., Kesavan, G., Wagner, K., Friedrichs, J. and Guck, J. (2019). Polyacrylamide bead sensors for in vivo quantification of cell-scale stress in zebrafish development. *Scientific Reports* **9**, 17031.

Von Dassow, M., Strother, J. A. and Davidson, L. A. (2010). Surprisingly simple mechanical behavior of a complex embryonic tissue. *PLoS ONE* **5**, 958-966.

Weber, G., Bjerke, M. and DeSimone, D. (2012). A mechanoresponsive cadherin-keratin complex directs polarized protrusive behavior and collective cell migration. *Developmental Cell* **22**, 104–115.

Wells, R. (2013). Tissue mechanics and fibrosis. *Biochimica et Biophysica Acta: Molecular Basis of Disease* **1832**, 884–890.

Xiong, Y., Lee, A., Suter, D. and Lee, G. (2009). Topography and nanomechanics of live neuronal growth cones analyzed by atomic force microscopy. *Biophysical Journal* **96**, 5060-5072.

Figures

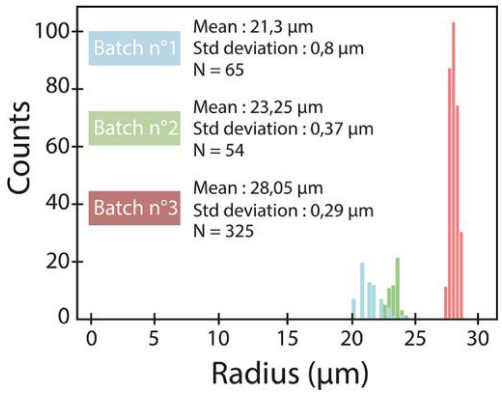

Figure 1. Distribution of microsphere's radii for three different batches obtained with a microfluidic device.

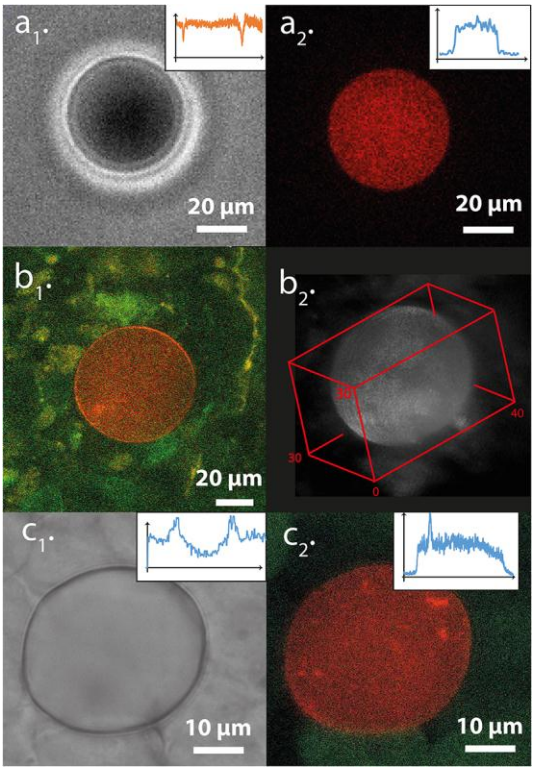

Figure 2. Images of three sensors in different situations: (a) suspended in water; (b) embedded in a CT26 reconstituted aggregate (green); (c) implanted in a zebrafish embryo (green). (a1) and (c1) are bright field images. (a2) is obtained with a spinning-disk, (b1) with a 2-photon and (c2) with a confocal microscope; (b2) is a 3D reconstruction obtained with ImageJ software. The insets represent the intensity profile through the sensor's diameter

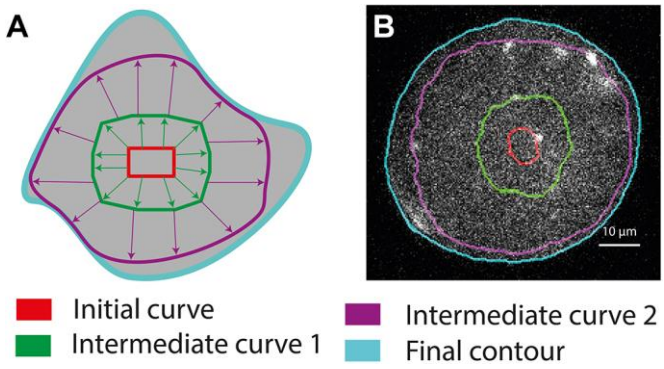

Figure 3. Determination of the sensor's contour; (a) Principle of the active contour method: the initial seed (red) progressively swells (green, purple), until it reaches the contour of the object (cyan), which minimizes its pseudo-energy (see text). (b) Example of contour determination for a sensor inserted in an aggregate (same color code as (a)).

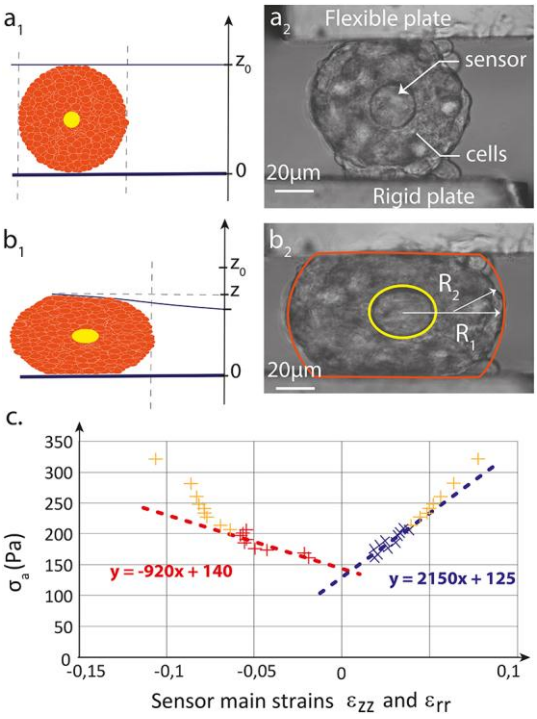

Figure 4. In situ calibration of a sensor shear modulus in an aggregate. Principle (a1, b1): a CT26 cell aggregate, initially spherical and containing a sensor at its center, is squeezed between two glass plates. The images (a2, b2) are analyzed to extractthe sensor main strains ε_{zz} and ε_{rr}. (c) Variations of the average stress $\sigma_a(t)$ *vs* $\varepsilon_{zz}(t)$ (red crosses) and $\varepsilon_{rr}(t)$ (blue crosses) during the relaxation of a squeezed aggregate. Yellow points are recorded during the first ≈ 30 s of the relaxation. The shear modulus μ_e of the sensor can be extracted from the slopes of the straight lines (Eq.12).

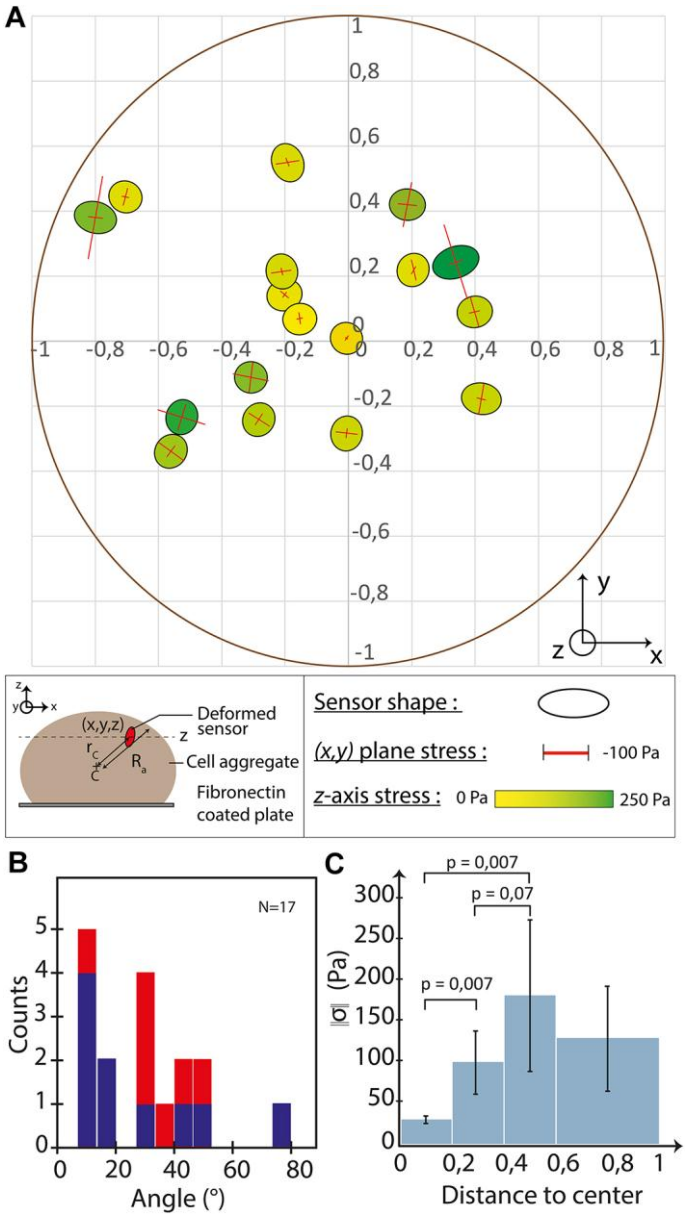

Figure 5. (a) Stress distribution map in CT26 aggregates, from 17 sensors inserted in 13 different aggregates. Each sensor is set at its normalized position $r = r_c / R_a$. Its shape projected in the (x, y) plane is represented by an ellipse (the ellipticity is multiplied by a factor 4 to make it more visible). The main shear stress components in the (x, y) plane are shown as red bars, while the projection of the stress in the z direction is represented by a color code. Note that the apparent elongation of the sensors in the z direction ($\sigma_{zz} > 0$) might be an artefact related to the imaging method (see Discussion) . (b) Distribution of angles between the radial direction and the sensor longer axis direction (blue: sensors showing a difference in half axes larger than the estimated accuracy $0.5\ \mu m$; red: other sensors). The sensors are principally compressed in the orthoradial direction. (c) Histogram of the shear stress amplitude $\|\sigma\|$ versus normalized distance to the center r . The error bars represent the standard deviation .

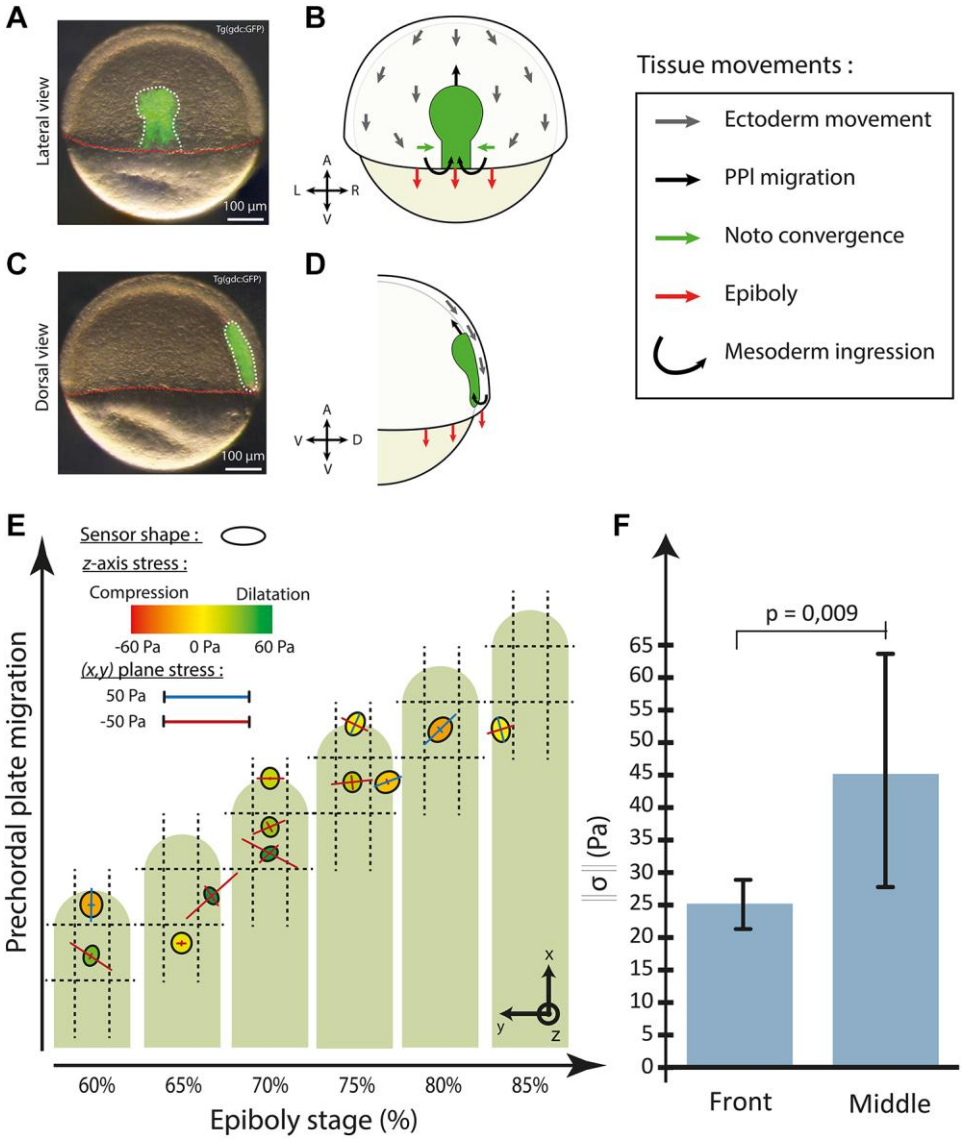

Figure 6. Measurements of the shear stresses in the zebrafish prechordal plate (PPl) during epiboly. (a-d): Ectoderm, prechordal plate (PPl) and notochord precursors (Noto) movements during gastrulation. (a,c) Bright fields and fluorescence images of a zebrafish Tg(gsc:GFP) embryo at 60% epiboly. Prechordal plate and notochord cells, expressing GFP in this transgenic line, are highlighted by the white dashed line. Red dashed line marks the margin of the embryo. (b,d) Schematics of corresponding pictures showing morphogenetic movements of the different tissues during gastrulation. Crossed arrows indicate animal-vegetal (A-V), left-right (L-R) and dorsal-ventral (D-V) embryonic axes of respective view. Panels a, b, c and d have been inspired by Smutny et al. (2017). (e) Mapping of shear stresses in the PPl at different epiboly stages (12 measurements on 7 different embryos). The projection on the (x, y) plane of the main shear stresses is drawn as an ellipse, while the projection along the axis z normal to the PPl (and confounded with the optical axis) is represented by a color code. (f) Comparison of the shear stress amplitude $\|\sigma\|$, averaged at the front ($N = 3$) and in the middle ($N = 7$) of the PPl. The error bars represent the standard deviation .

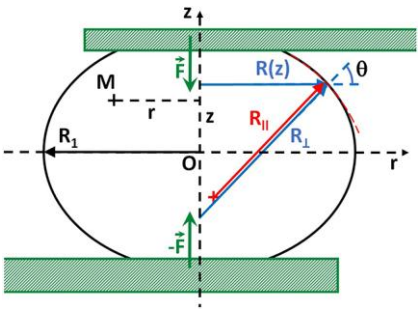

Figure 7. Scheme of a squeezed aggregate, assumed to respect cylindrical symmetry around Oz. The current point M is identified by its coordinates (r, ϕ, z) where ϕ is the azimutal angle; $R(z)$ is the radius of the curve generating the aggregate cylindrical surface; $R_{\perp}$ and $R_{\parallel}$ are the principal curvature radii; R_1 is the equatorial value of $R(z)$; $\vec{F}$ is the force exerted by the plates on the aggregate.

Table 1. Comparison of the average value $\overline{\mu}_e$, measured *in situ*, and μ_d, measured for a coarse emulsion of the same gel. Experiments have been performed on two gels having slightly different compositions.

	$\overline{\mu}_e$ (Pa)	μ_d (Pa)
Gel 1	730 ± 250 ($N = 9$)	710 ± 150
Gel 2	320 ± 100 ($N = 3$)	410 ± 70

Electronic Supporting Information

Chemicals.
Vinyl terminated polydimethylsiloxane (CAS n° 68083-19-2, 200 cSt, ref DMS-V22, MW=9400 g/mol) and (45-55% methylhydrosiloxane)-dimethylsiloxane copolymer, trimethylsiloxane terminated (CAS n° 68037-59-2, 10-55 cSt, ref HMS-501, MW=900-1200 g/mol) were purchased from Gelest. Karstedt's catalyst (Platinum(0)-1,3-divinyl-1,1,3,3-tetramethyldisiloxane complex solution in xylene, Pt ~2%, CAS N° 68478-92-2), diallyl maleate (93%, CAS N° 999-21-3), rhodamine B isothiocyanate (mixed isomers, CAS N° 36877-69-7) and allylamine (98%, CAS N° 107-11-9) were purchased from Sigma Aldrich. All chemicals were used as received without further purification.

PDMS precursor mix.
In a typical reaction, 30 g DMS were inserted into a 50 mL falcon centrifugal tube. The remaining components of the polymerizable mix were subsequently added directly into the tube while controlling the added mass on a scale so as to avoid losses on glassware. The mixture was homogenised using a vortex mixer after each addition for at least 60 s. 24 mg diallyl maleate ($3.82.10^{-2}$ eq per DMS strand), 128 mg of Karstedt's catalyst solution ($4.13.10^{-3}$ eq Pt per DMS strand) and 459 mg hydrosilane cross-linker ($1.37.10^{-1}$ eq per DMS strand) were added sequentially. It is essential that the cross-linker be added last to avoid the reaction starting in uncontrolled conditions. The as-prepared mixture needs to be stored at 4°C and should be used within a few days least the cross-linking reaction significantly moves forward. The mix can then be used as a feedstock for microdroplet fabrication or be directly cured at 80°C for 3 hours in a stove.

Synthesis of the vinyl-terminated Rhodamine B analog.
A 0.93 mM stock solution of rhodamine B isothocyanate was prepared by dissolving 5.0 mg in 10 mL of chloroform. A 58 mM stock solution of allylamine was prepared by dissolving 50 mg in 15 mL of chloroform. In a 20 mL scintillation vial, 3.0 µmoles of RhB-ITC (3.22 mL stock) were mixed with 3.3 µmoles allylamine (1.1 eq., 93 µL). The reaction mixture was diluted up to 15 mL using chloroform and was left to stir overnight in the sealed vial. The obtained vinyl-terminated rhodamine B analogue solution can be used straight away for labelling of DMS. The scale reaction is described at a scale suited for fluorescent labelling of 30 g of DMS-V22 at a ratio of one fluorescent label for 1,000 DMS strands.

Fluorescent labelling of PDMS.
The above-described 200 µM vinyl-terminated Rhodamine B analogue solution was added to 30 g of DMS in a 50 mL Falcon centrifugal tube. The mix was first homogenised using a vortex mixer. It was subsequently shaken using an ultrasonic horn for 4 min under a fumehood. During the ultrasonication, the tube was nested in an ice bath to avoid overheating the mixture. To eliminate the remaining chloroform, the mix was then transferred to an Erlenmeyer flask and stirred using a magnetic bar for 2 hrs under the hood. The fluorophore-doped DMS could then be used in the same way as plain DMS for the preparation of a polymerizable mix (the contribution of the fluorophore to the mass was neglected when calculating the needed mass of the other components).

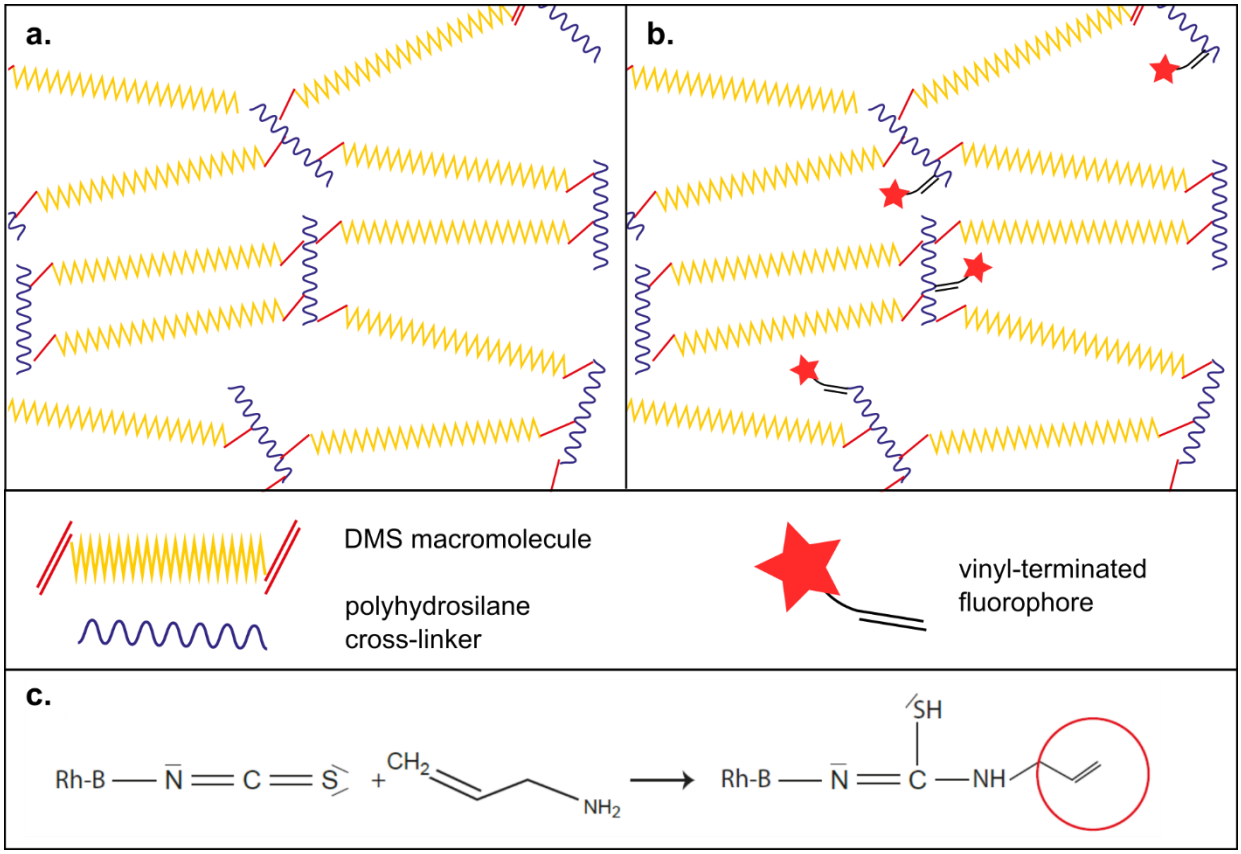

Fig. S1. Schematics of the gel meshwork: (a) Plain PDMS, (b) fluorescently labelled PDMS. (c) The vinyl-terminated rhodamine B analogue is obtained from the condensation of RITC and allylamine.

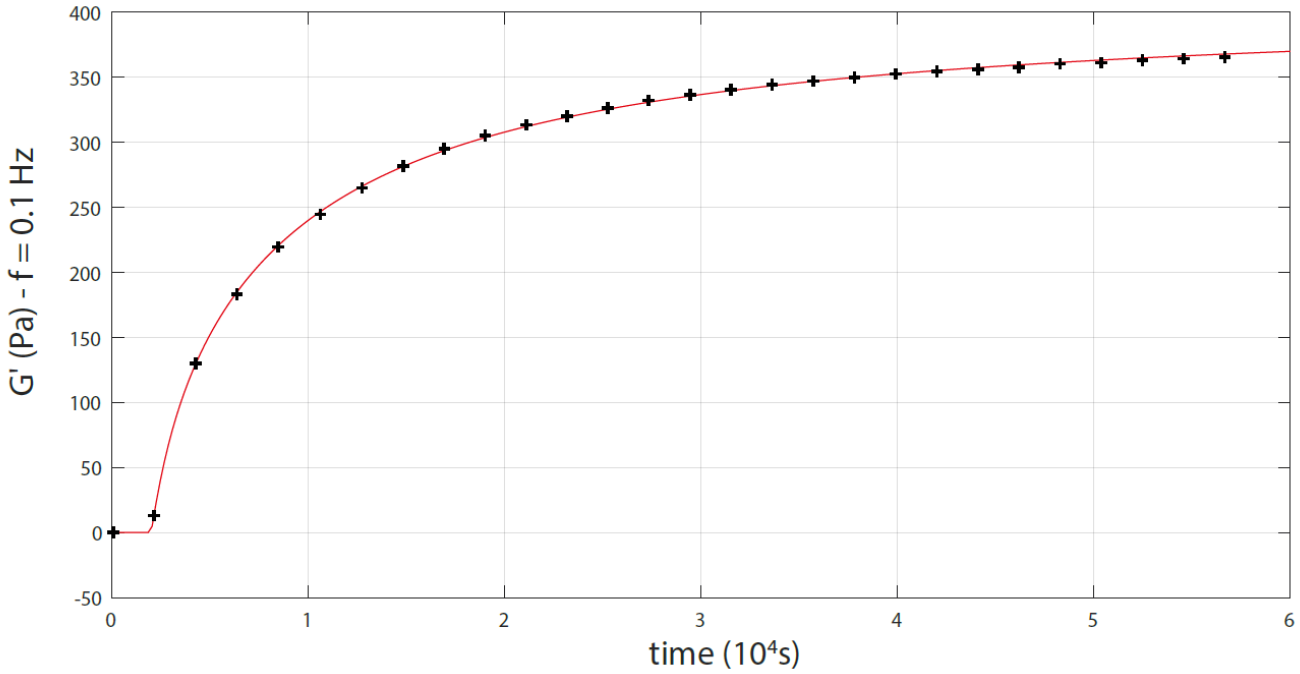

Fig. S2. Storage modulus G'(t) of the polymerization mixture measured as a function of time, at fixed frequency f = 0.1Hz and fixed temperature T= 60°C, in a cone-plate geometry. Here G' tends towards an asymptotic value $G'_f \approx 400$ Pa after 17h. The red line represents the fit based on Flory's theory of gelification, as described in detail in Alexandre Souchaud's PhD thesis (Souchaud, 2020) and in P.J. Flory, Molecular Size Distribution in Three Dimensional Polymers. 1- Gelation, JACS 63: 3083 (1941).

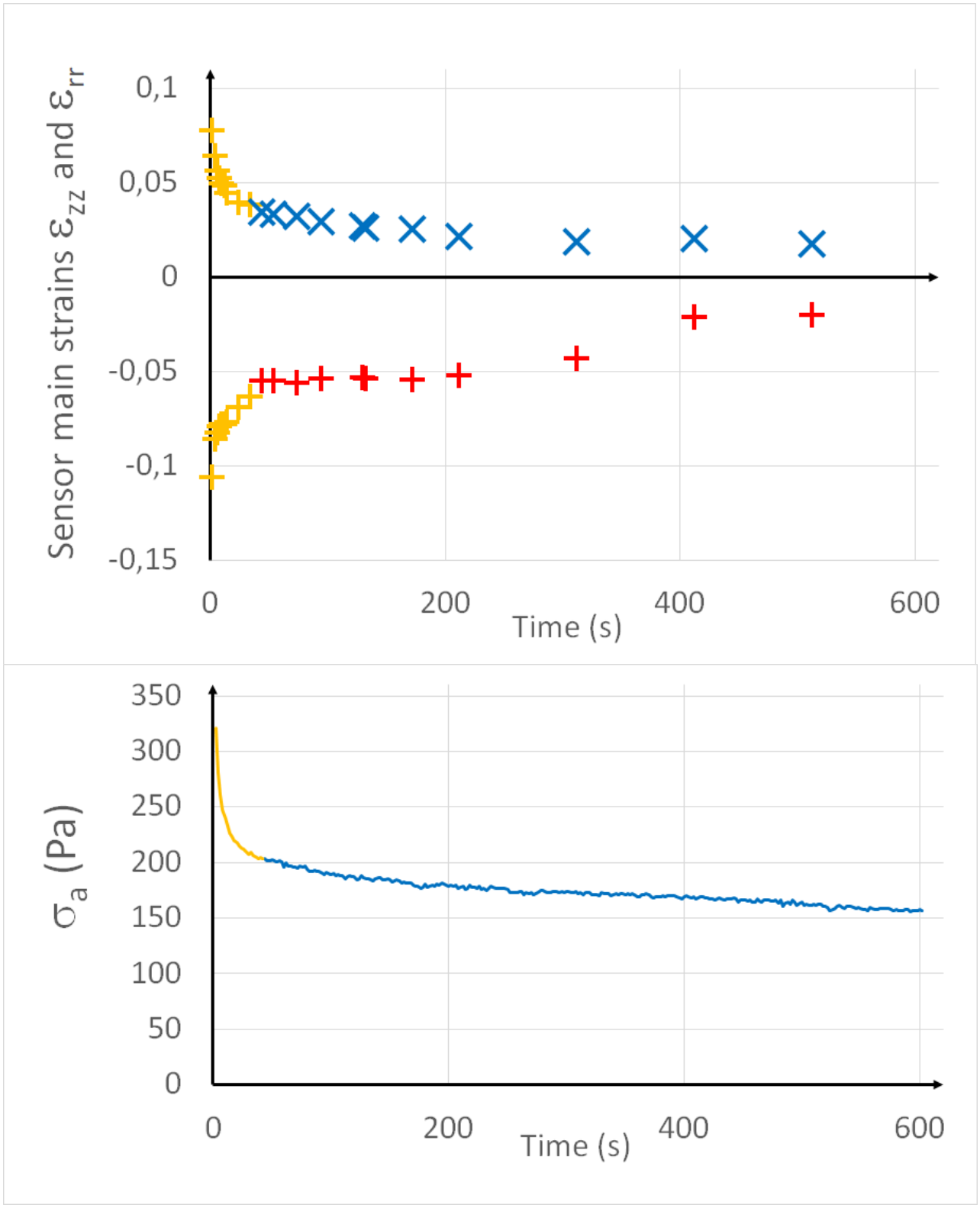

Fig. S3. Evolution of ε_{zz}, ε_{rr} and σ_a as a function of time after a compression step of the aggregate (same data and same color code as in Figure 4). During the first 30 s (yellow points), both the average stress and the sensor deformation relax rapidly, due to quick intercellular and intracellular relaxation processes. In this regime it is likely that the stresses are not homogeneous in the aggregate. Later (red and blue points), the relaxation becomes slower. One then assumes that σ_{zz} is homogenous in a plane orthogonal to the symmetry axis, so that the model developed in the appendix applies.

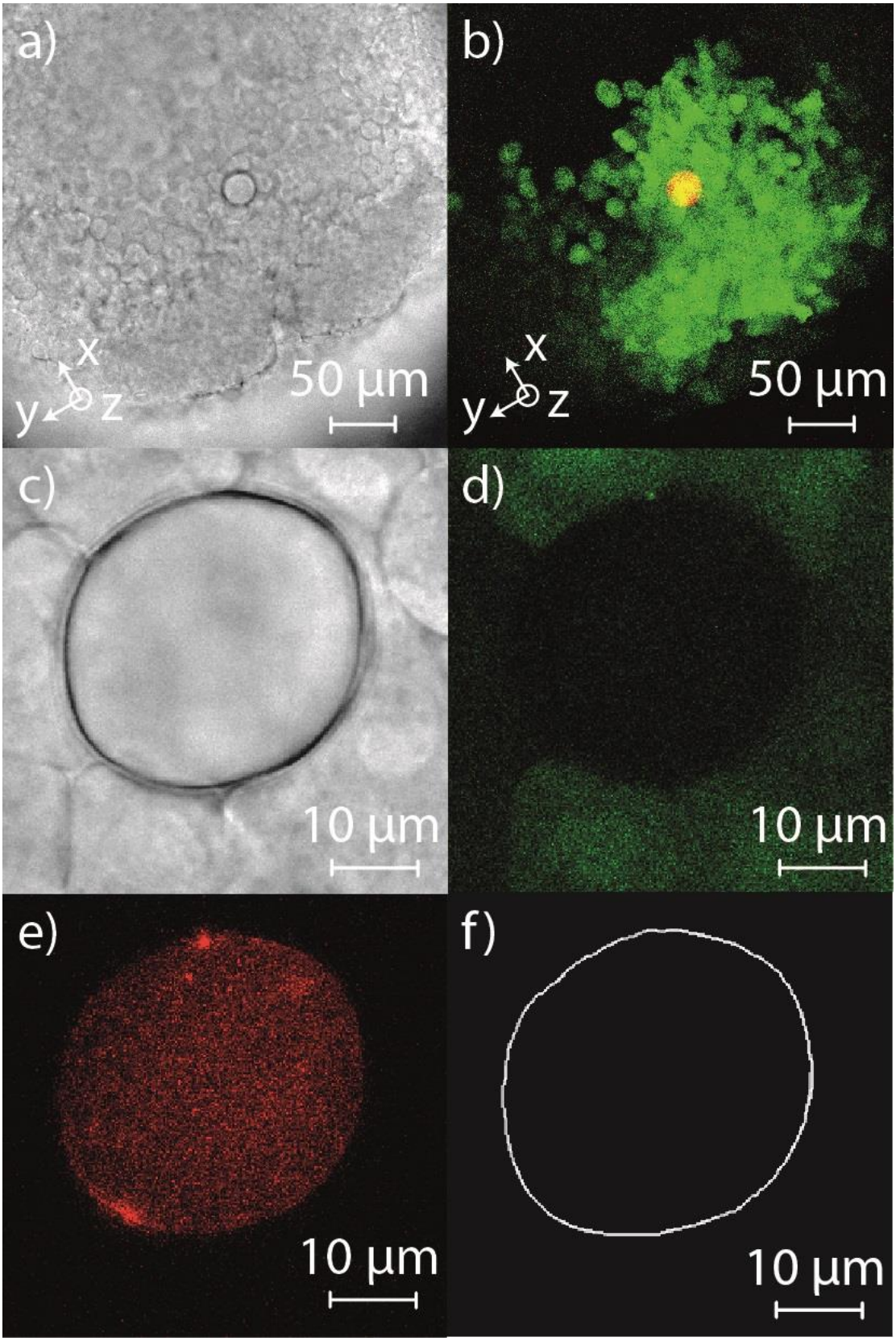

Fig. S4. Raw images of a sensor implanted in the PPl of a Zebrafish embryo; a) and b) Overview of the sensor inside the embryo ; a) Bright field, b) Superimposition of the fluorescence images of the sensor (rhodamin labelled) and of the PPl cells (GFP transfected); c) to e) : zoom on the sensor ; c) bright field ; d) GFP channel; e) Rhodamin channel; f) Sensor contour determined by the active contour method. The xyz coordinate system is identical to the one shown in Fig. 6e.

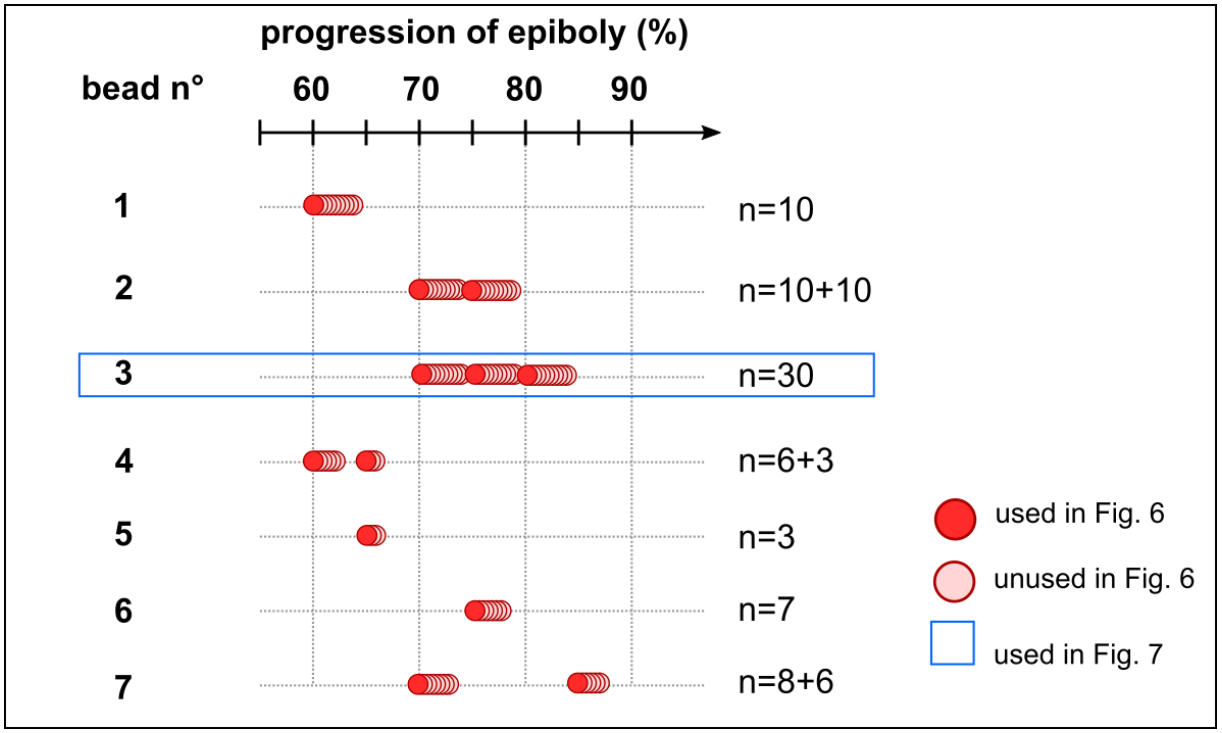

Fig. S5. Overview of the dataset acquired on zebrafish embryos. Each circle represents a stack of images, collected at a given stage of epiboly. Red-filled circles highlight data featured in Fig. 6, selected to have maximum spread over the progression of epiboly. The time series featured in Fig. 7 is highlighted by a blue frame (bead 3, n=30).

Example of time evolution:

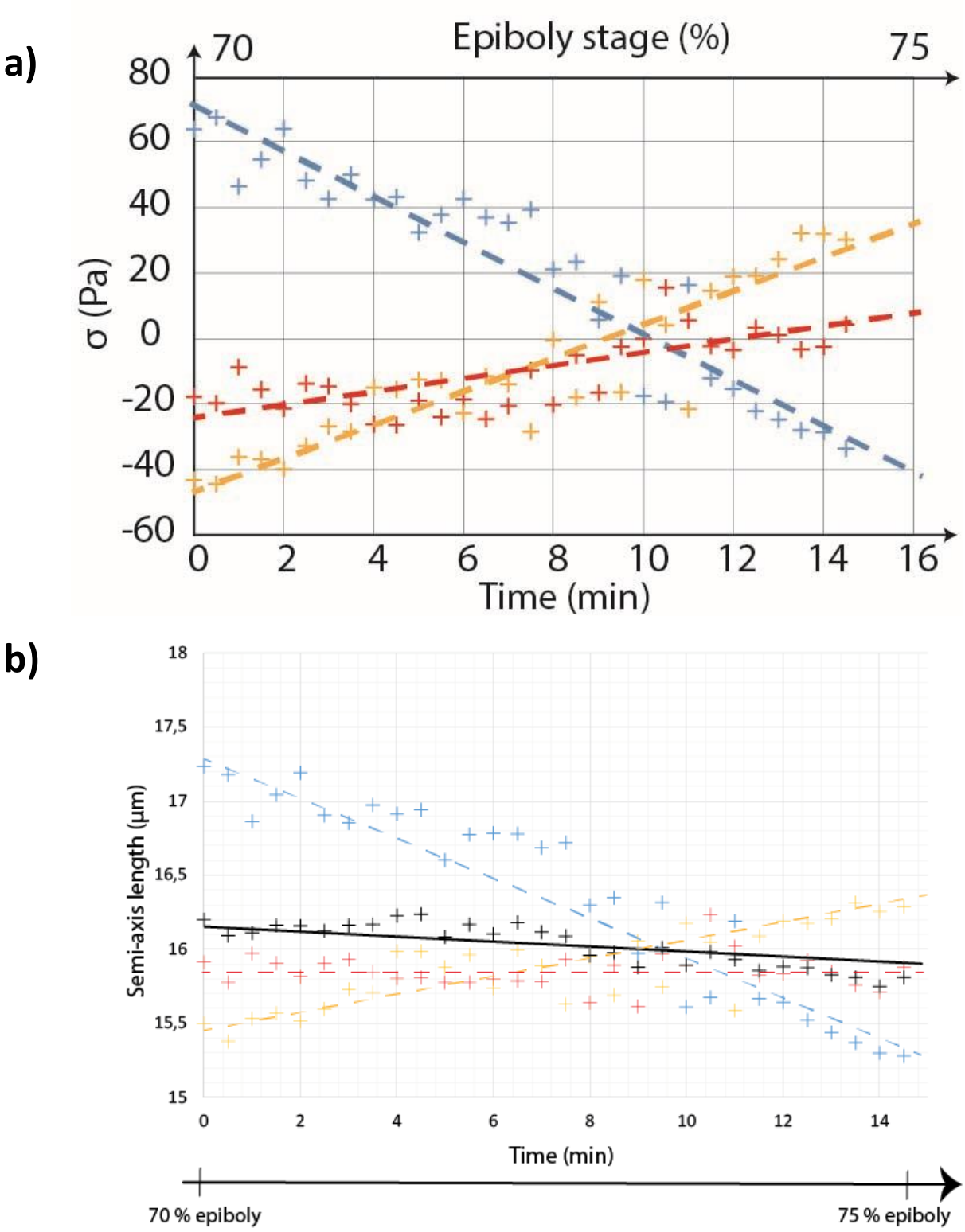

Fig. S6. a) Time evolution of the main components σ_{XX}, σ_{YY} and σ_{ZZ} of the shear stress tensor exerted on a sensor located in the central zone of the PPl of a zebrafish embryo. Each principal axis X, Y, Z is color-labelled according to its nearest axis x, y or z of the PPl referential. Dashed lines are guides for the eye ; b) Plot of the evolution of the three half-axes length a_X, a_Y and a_Z for a deformed sensor (same sequence and same color code as in a)), together with the radius R of a sphere having the same volume (black crosses). R is stable with time, as compared to the variations of the half-axes.

Amongst the 7 sensors inserted in the PPl, and migrating with it, that we could follow with time, one exhibited a visible evolution. This sensor was imaged during 15 min, at the stage 70 - 75% of epiboly. In Fig. S6a, the three main components σ_{XX}, σ_{YY} and σ_{ZZ} of the shear stress exerted on the sensor are plotted versus time. Within 15 minutes, the stress amplitude along the principal axis closest to the z axis (blue) changes from positive (extension) to negative (compression). In the same time interval, the stress along the axis closest to the y axis follows the opposite evolution (yellow), and so does, to a lesser extent, the component close to x axis (red). Their directions remain stable except for some small fluctuations.

We argue that this event cannot be an experimental artifact related to image analysis uncertainty. Indeed, we have plotted in Fig. S6b the evolution of the three half-axes a_X, a_Y and a_Z of the deformed sensor, together with the radius $R= (a_X\, a_Y\, a_Z)^{1/3}$ of the sphere of same volume. It shows that R is stable with time, as compared to the variations of the half-axes. Thus, the sensor volume remains constant during this sequence, while its shape changes, and consequently so does the shear stress exerted on it.

This evolution takes place within a few minutes at this stage of epiboly. Its duration is short as compared to the gastrulation characteristic time, which might explain why it has been observed only once, out of 7 assays. Of course, we do not have enough information to allow any biological interpretation of this single event. Nevertheless, its occurrence suggests that the pipeline enables to follow the time evolution of the shear stress tensor during the prechordal plate migration.

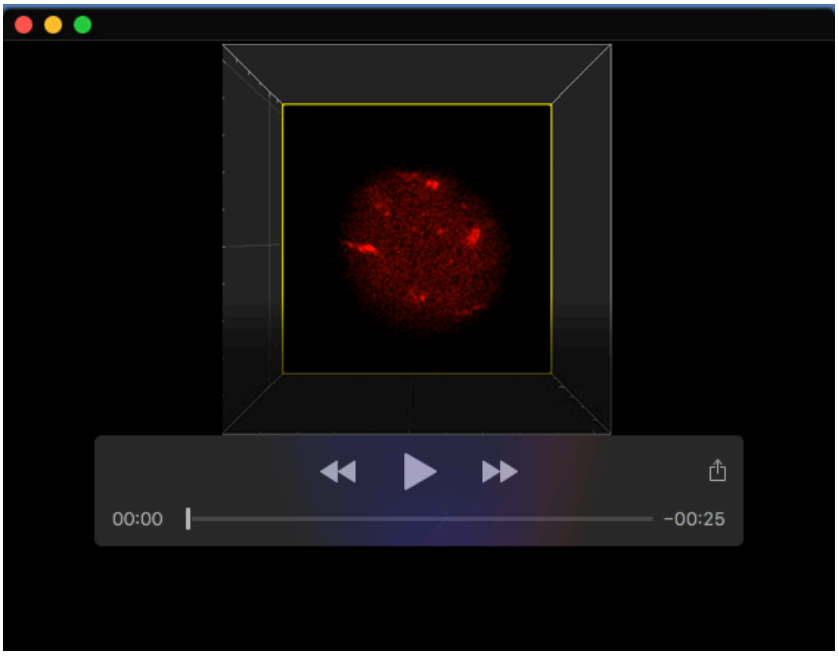

Movie 1. Example of reconstruction of the 3D shape of a bead by the active contour method.
Rotating view of a bead inserted in the Zebrafish prechordal plate. Red: raw 3D image from confocal stacks. Green: contour calculated by the active contour method. Blue: best fit by an ellipsoid.